Afonso da Cunha Ferreira

Licenciado em Ciências de Engenharia de Micro e Nanotecnologias

Perylene Diimide acceptors: Fabrication and characterization of electron-only, hole-only devices and solar cells

Dissertação para a obtenção do Grau de Mestre em
Engenharias de Micro e Nanotecnologias

Orientador: Paul Blom, Professor Doutor,
Max Planck Institute for Polymer Research

Co-orientador: Isabel Ferreira, Professora Doutora,
Faculdade de Ciências e Tecnologia da Universidade Nova de Lisvoa

Júri:

Presidente: Prof. Doutor Rodrigo Ferrão de Paiva Martins
Arguente: Prof. Doutor Luiz Fernando Ribeiro Pereira
Vogal: Prof. Doutora Isabel Maria Mercês Ferreira

Novembro, 2015

FACULDADE DE
CIÊNCIAS E TECNOLOGIA
UNIVERSIDADE NOVA DE LISBOA

Perylene Diimide acceptors: Fabrication and characterization of electron-only, hole-only devices and solar cells

Acknowledgments

I would like to start off by sending a sincere thank you to everyone who helped me throughout my academic years and in my dissertation. It has been a challenging but rewarding time in my life. I realize that it will not be possible to mention every single person from these 5 years and I apologize to those who I forgot to include in these acknowledgments, however I will try to make justice to everyone.

First of all, I would like to thank Dr. Paul Blom and Dr. Irina Crăciun for giving me the opportunity to work alongside such an amazing team at Max Planck Institute for Polymer Research (MPIP), in an institute and research group with great recognition in the field, and for an experience that will not be forgotten. Thank you for your support and knowledge input during my time there.

Also a special thanks to Selen for all your help and mentoring. Thank you for all your patience while introducing me to a research topic I was not too much familiar with and for guiding me almost every day and teaching me the ropes of conducting proper scientific research.

Thank you so much to my co-advisor, professor Dr. Isabel Ferreira, that besides the distance was always ready to help in any problem that I encountered. Thanks for being such a good teacher, for all those long meetings helping me understand and analysing results and specially for the last minute rescues. The last few weeks were very stressful but the professor was very supportive and available. I thank you again.

A big thanks to all my friends from across the world that I met in Erasmus. You already know that you have a permanent couch here in Portugal and I hope to continue seeing you guys for years to come. A-town friends forever.

Thanks to my colleagues and friends who I have met at university and who have accompanied me from the start. A special mention to both the original and adopted members of the iconic house "Basolho", that became really close friends of mine and with whom I have shared wonderful moments. Çim.

Also I could not help but to send a huge, huge hug to all the "gang" from Queijas and outskirts and life-long best friends. I don't think I need to say who you are because you all already know. We are all stepping into a different phase in our lives that is full of uncertainty and where we may not see each other all the time, but I know for sure that this friendships will endure. É para a vida "mos putos".

And of course, last but most importantly, an unmeasurable thank you to my entire family. In particular to my brother and sister for putting up with me and the "injustices" that come with having a big brother, and my parents for their endless love, support and sacrifices that made all the opportunities and experiences of my short life possible.

Abstract

The thrust towards energy conservation and reduced environmental footprint has fueled intensive research for alternative low cost sources of renewable energy. Organic photovoltaic cells (OPVs), with their low fabrication costs, easy processing and flexibility, represent a possible viable alternative. Perylene diimides (PDIs) are promising electron-acceptor candidates for bulk heterojunction (BHJ) OPVs, as they combine higher absorption and stability with tunable material properties, such as solubility and position of the lowest unoccupied molecular orbital (LUMO) level. A prerequisite for trap free electron transport is for the LUMO to be located at a level deeper than 3.7 eV since electron trapping in organic semiconductors is universal and dominated by a trap level located at ~3.6 eV. Although the mostly used fullerene acceptors in polymer:fullerene solar cells feature trap-free electron transport, low optical absorption of fullerene derivatives limits maximum attainable efficiency. In this thesis, we try to get a better understanding of the electronic properties of PDIs, with a focus on charge carrier transport characteristics and the effect of different processing conditions such as annealing temperature and top contact (cathode) material. We report on a commercially available PDI and three PDI derivatives as acceptor materials, and its blends with MEH-PPV (Poly[2-methoxy-5-(2-ethylhexyloxy)-1,4-phenylenevinylene]) and P3HT (Poly(3-hexylthiophene-2,5-diyl)) donor materials in single carrier devices (electron-only and hole-only) and in solar cells. Space-charge limited current measurements and modelling of temperature dependent J-V characteristics confirmed that the electron transport is essentially trap-free in such materials. Different blend ratios of P3HT:PDI-1 (1:1) and (1:3) show increase in the device performance with increasing PDI-1 ratio. Furthermore, thermal annealing of the devices have a significant effect in the solar cells that decreases open-circuit voltage (V_{OC}) and fill factor FF, but increases short-circuit current (J_{SC}) and overall device performance. Morphological studies show that over-aggregation in traditional donor:PDI blend systems is still a big problem, which hinders charge carrier transport and performance in solar cells.

Resumo

O recente impulso para a conservação de energia e redução da pegada ambiental tem vindo a alimentar intensa investigação ciêntifica por fontes alternativas de energia renovável e de baixo custo. Células fotovoltaicas orgânicas (OPVs), tendo custos de fabricação baixos, sendo de fácil processamento e permitindo dispositivos mecânicamente flexíveis, representam uma possível alternativa viável. Derivados de perileno diimida (PDIs) são candidatos promissores para a substituição de derivados de fulereno em células solares de heterojunção de volume (BHJ). Os PDIs combinam uma maior absorção e estabilidade com a possibilidade de ajustamento de certas propriedades do material, tais como a solubilidade e a posição da orbital molecular desocupada mais baixa (lowest unoccupied molecular orbital, LUMO). Um pré-requisito para o transporte de electrões livre de "armadilhas"energéticas é que o LUMO esteja abaixo de 3.7 eV, uma vez que o aprisionamento de electrões em semicondutores orgânicos é universal e dominado por um nível energético de armadilhamento localizado a $\sim$3.6 eV. Embora os fulerenos mais usados como material aceitador de electrões em células solares de sistemas polímero:fulereno disporem de um transporte de electrões livres de armadilhamento, a baixa absorpção óptica dos derivados de fulereno impõe um limite máximo na eficiência obtenível. O objectivo deste trabalho consistirá em obter uma melhor compreensão das propriedades eletrónicas dos PDIs (com foco no transporte de portadores de carga) e o efeito de diferentes condições de processamento, tais como o tratamento térmico, material do contacto superior (cátodo), entre outras. Nós reportamos sobre um PDI disponível comercialmente e três derivados de PDI como materiais aceitadores de electrões e a sua combinação com os materiais dadores de electrões, MEH-PPV (Poli [2-metoxi-5- (2-etilhexil oxi) -1,4-fenilenovinileno]) e P3HT (poli (3-hexiltiofeno-2,5-di-il)), em dispositivos com um único portador de carga (electrões, *eletron-only*, e buracos, *hole-only*) e em células solares. Medições de correntes limitadas por cargas espaciais e modelagem de características *J-V* dependentes de temperatura, confirmam que o transporte de eletrões, em tais materiais, é livre de armadilhamento. Misturas de P3HT:PDI-1 com diferentes proporções de (1:1 e (1:3) mostram um melhoramento no desempenho do dispositivo com o aumento da proporção de PDI-1. Além disso, o tratamento térmico dos dispositivos tem um efeito significativo nas células solares, efeito esse que diminui a tensão em circuito aberto (V_{OC}) e o *fill factor* (FF), mas que aumenta a corrente de curto-circuito (J_{SC}) e o desempenho geral do dispositivo. Estudos morfológicos mostram que o excesso de agregação em sistemas tradicionais de misturas dador:PDI é ainda um grande problema, que dificulta o transporte de portadores de carga e o desempenho em células solares.

Contents

List of Figures

List of Tables

Introduction

There is an ever-growing need to address both energy and environmental issues, product of generations of over-exploitation of fossil fuel sources and the increased associated industries, which represent one of the most beneficial and, at the same time, injurious aspects of modern times. Solar energy offers the advantages of being renewable and clean, thus making solar cells attractive as a prospective alternative energy source. Although still lacking in terms of efficiencies and lifetime, comparing to their inorganic counterparts, organic photovoltaic cells (OPVs) benefit from relatively low fabrication cost, easy processing, and flexibility [1–3]. The development of OPVs has progressed rapidly with the synthesis of new organic materials, control of processing condition such as annealing and the use of additives [4], as well as the introduction of various device structures such as the tandem and inverted structure [5, 6]. Within the line of thought of using new organic materials, Perylene diimides (PDIs) are promising electron-acceptor materials for fullerene-free bulk-heterojunction (BHJ) OPVs, and will be the main focus of this work.

This thesis fell within the ambit and in a way complements the undergoing PhD project of Organic Electronics and Photovoltaics, in the research group of Molecular Electronics of the Max Planck Institute for Polymer research (MPIP) in Mainz, Germany. In the work presented here, we examine a commercial PDI and three PDI derivatives as acceptor materials in fullerene-free organic photovoltaic cells with the purpose of getting a better understanding of their electronic properties, mainly their charge transport characteristics. OPVs and single carrier devices are fabricated, where we test different blend ratios of commercial PDI with MEH-PPV (Poly[2-methoxy-5-(2-ethylhexyloxy)-1,4-phenylenevinylene]) and P3HT (Poly(3-hexylthiophene-2,5-diyl)) donor materials, as well as different processing conditions (such as annealing temperature and top contact (cathode) material). Additionally, some atomic force microscopy (AFM) morphology work was carried out to study aggregation problems in PDI based films.

1.1   Conjugated polymers

Organic photovoltaics are made of electron donor and electron acceptor materials rather than semiconductor p-n junctions. The molecules forming the electron donor region of organic PV cells, where exciton electron-hole pairs are generated, are generally conjugated polymers possessing delocalized π electrons that result from carbon p orbital hybridization (see figure 1.1). These π electrons can be excited, by light in or near the visible part of the spectrum, from the molecule's highest occupied molecular orbital (HOMO) to the lowest unoccupied molecular orbital (LUMO), denoted by a $\pi - \pi^*$ transition. The energy bandgap between these orbitals determines which wavelength(s) of light can be absorbed [7].

In a semiconductor polymer film, not all molecules are equally long (variety in chain length), and their chains are not perfectly straight (kinks in the chain). This makes conjugated polymers disordered, with a distribution of the HOMO and LUMO levels, and therefore, the concept of band conduction does not apply. Instead, as mentioned before, localized states are formed and charge carriers are able to "jump" from one state to another. This type of charge transport is described as a hopping process/transport, which in contrast with band transport, can be thermally activated and assisted by vibrations and phonons, in order to overcome the energy difference between such states [8, 9].
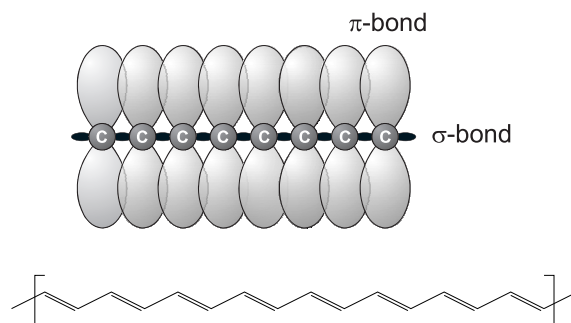
Figure 1.1: *Schematic representation of the electronic bonds between carbon atoms (above) and the chemical structure of polyacetylene, comprising of alternating single and double bonds between the carbon atoms (below). Adapted from [10].*

The conversion of photon energy into free charge carriers is explained by the following steps (also illustrated in figure 1.2, where the structure of a typical BHJ solar cell can be seen, followed by the correspondent energy-band diagram in figure 1.3):

- Light is absorbed in the donor material and thus excitons (i.e. strongly bound electron-hole pairs) are created in the polymer chain. Conjugated polymers have very high absorption coefficients, but, only narrow absorption bands, which can be circumvented by novel materials and/or multijunction (tandem cells) systems;

- The photogenerated excitons are strongly Coulomb bound due to the low dielectric constant in organic materials, and the correspondingly low screening length. These need to be dissociated and in order for that they need to reach an acceptor site, which is done only by diffusion. However excitons have very short diffusion lengths, reason why for the use of bulk-heterojunction solar cells, which consists of an intermixed system of donor and acceptor materials;

- If the acceptor material/molecule is energetically favorable (i.e. the energy gain is bigger than the exciton binding energy) dissociation takes place, sending an electron into the acceptor and leaving a hole in the donor polymer. A polaron pair is formed;

- This pair still needs to be dissociated (since it is still Coulombically bound). This time, dissociation is assisted by an electric field (composed of built in voltage, plus an applied voltage), therefore photocurrent strongly depends on applied voltage;

- Finally the electrons and holes are transported to the respective electrodes, driven by the electric field, and moved by the hopping transport process, where they can then be collected;
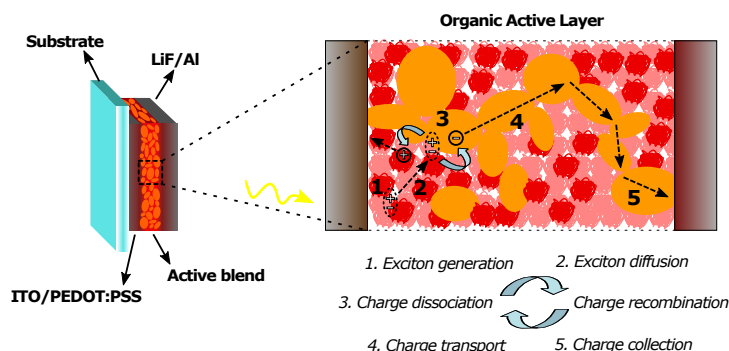
Figure 1.2: *Schematic layout of a typical bulk-heterojunction solar cell. A section of the active layer is enlarged to illustrate the processes of light absorption and charge generation/collection.*
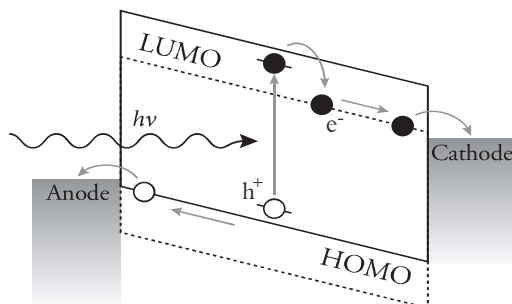
Figure 1.3: *Schematic energy-band diagram of a bulk-heterojunction organic solar cell. The solid lines represent the energy levels of the donor, while the dashed lines represent the energy levels of the acceptor. Adapted from [11].*

1.1.1 Carrier transport

Charge carrier transport properties are a important part of a solar cell characterization. The electron and hole transport should be measured separately and for this purpose, single carrier devices are often used. These are fabricated by selectively blocking the carriers of opposite sign by changing the work function of the relevant contacts. For hole-only (HO) devices, a high work-function metal like gold (Au) is used as top contact. As for electron-only (EO) devices, to suppress/block hole injection, one can use a thin oxide barrier, such as aluminum oxide (Al_2O_3) for the bottom contact. A schematic representation of single carrier devices can be seen in 1.4. In such devices, a space-charge limited current (SCLC) is often observed. This is because when a semiconductor polymer layer is contacted by an ohmic contact that can readily inject a large number of charge carriers and another electrode that can extract these charges, the current flow will be limited by a buildup of space charge due to the low carrier mobility found in such materials. The total amount of charge carrier injected into the insulator is linearly proportional with the voltage. The current is given by the amount of charges multiplied by their velocity. Since both the amount of charges as well as the velocity (mobility × electric field) are linearly proportional with the voltage, this results in a quadratic dependence of the current density on voltage. Considering only one charge carrier, the SCLC density flowing across a layer with thickness L is given by [12, 13]

$$J_{\text{SCL}} = \frac{9}{8}\epsilon\mu\frac{V_{int}^2}{L^3} \tag{1.1}$$

where ϵ is the dielectric constant of the material (estimated to be 3 for organic semiconductors), μ the carrier mobility and V_{int} the internal voltage in the device. Electrostatically there is a limit for the build up of space charge in a semiconductor when the integral of the space-charge induced field over the semiconductor thickness is equal to the applied voltage. Then, the SCLC is reached, which is the maximum current that can be sustained. The internal voltage drop

(a) *Hole-only device*

(b) *Electron-only device*
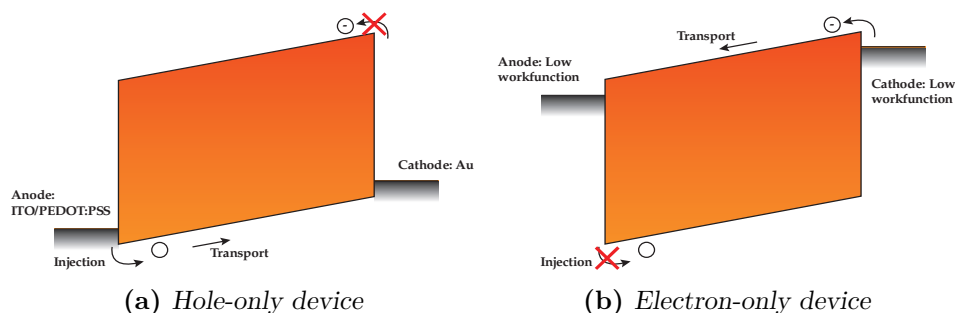
Figure 1.4: *Schematic energy level diagrams in single carrier devices. Both are under forward bias [14].*

across the active layer is related to the applied voltage V_a by

$$V_{int} = V_a - V_{bi} - V_{Rs} \tag{1.2}$$

where V_{bi} is the built-in voltage which arises from the difference in work function of the bottom and top electrode and V_{Rs} is the voltage drop across the series resistance of the substrate. The built-in voltage is determined from the *J-V* characteristics as the voltage at which the characteristic becomes quadratic, corresponding to the SCL regime. For organic semiconductors the SCLC equation 1.1 is only valid at low voltages. At higher voltages the charge carrier mobility increases with increasing electric field and carrier density, ρ. As a result the current is no longer quadratic with voltage, but increases more rapidly. In one of his works Pasveer *et al.* [15] established a unified theoretical description of the full T, ρ an E dependence of μ:

$$\mu(T, \rho) = \mu_0(T) \ exp \left[\frac{1}{2}(\sigma^2 - \sigma)(2\rho a^3)^\delta \right] \tag{1.3a}$$

$$\mu(T) = \mu_0 c_1 \ exp \left[-c_2 \sigma^2 \right] \tag{1.3b}$$

$$\delta \equiv 2\mu \ \frac{ln(\sigma^2 - \sigma) - ln(ln4)}{\sigma^2}, \ \mu_0 \equiv \frac{a^2 v_0 e}{\sigma} \tag{1.3c}$$

with $c_1 = 1.8 \times 10^{-9}$, $c_2 = 0.42$, and where $\sigma \equiv \sigma/k_B T$ (σ represents the width of the Gaussian distribution of localized states), a is the site spacing/lattice constant. This parametrization is particulary true for not too high densities.

1.1.2 Electronic trapping in organic semiconductors

In many organic semiconductors a big limiting factor is the presence of electronic traps. The exact origin of such trap states is still in debate, but the main proposed sources are impurities, structural defects, geminate pairs and self-trapping in intermolecular states [16]. Traps affect strongly the charge transport properties since trapped charge carriers do no longer take part in the charge transport. However, their columbic charge will influence the electric field distribution in a device and therewith the transport. Further, if the release rate for trapped carriers is sufficiently low, there will be a significant time necessary to reach quasi-thermal equilibrium conditions. This causes delay and hysteresis effects in alternately operated devices. A prerequisite for trap free electron transport is that the LUMO should be deeper than 3.7 eV since electron trapping in organic semiconductors is universal and dominated by a trap level at ∼3.6 eV [17]. Therefore, having a LUMO level at ∼3.8 eV with PDI-1, should allow for trap-free electron transport. Traps also act as recombination centers, being recombination of electrons
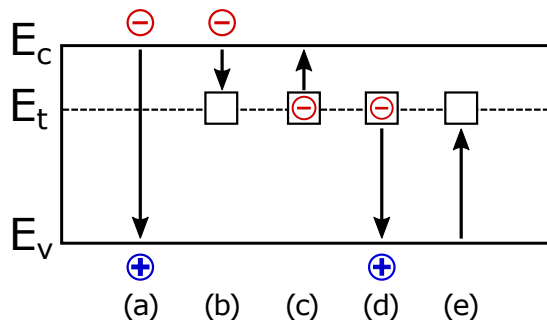
Figure 1.5: *Schematic representation of bimolecular recombination and the four processes involved in recombination by trapping: (a) bimolecular, Langevin recombination, (b) electron capture, (c) electron emission, (d) hole capture, and (e) hole emission. Adapted from [18].*

and holes, a process by which both carriers are annihilated. The main two mechanisms of re-combination are bimolecular and trap-assisted recombination, which are illustrated in figure 1.5. Bimolecular recombination (figure 1.5a), also known as non-geminate recombination, is usually considered to be of the Langevin-type. Direct band-band recombination of free carriers does not exist as such in organic disordered semiconductors, so, for two oppositely charged carriers to recombine, they first have to find each other [19, 20]. That is described by the Langevin re-combination rate. Trap-assisted recombination, i.e. Shockley-Read-Hall (SRH) recombination, is a two-step process where a trap state captures a charge carrier that subsequently recombines with a mobile carrier of the opposite sign due to their Coulombic interaction. This process is illustrated in figure 1.5b-d and is often described by the following recombination rate

$$R_{SRH} = \frac{C_n C_p N_t n p}{C_n \left(n + n_1 \right) + C_p \left(p + p_1 \right)} \tag{1.4a}$$

$$p_1 n_1 = N_{cv} \, exp \left(-\frac{E_{gap}}{kT} \right) \tag{1.4b}$$

where C_n and C_p are the capture cross sections for electrons n and holes p, respectively. N_{cv} is the effective density of states; N_t is the density of electron traps; and $p_1 n_1$ follows the relationship shown in equation 1.4b [18].

1.2   Device characteristics of organic solar cells

An organic solar cell based on conjugated polymers consists on, the later, being sandwiched between two electrodes with asymmetric work function. To determine the performance of a solar cell, the device is characterized in dark and under illumination. An example of a typical *J-V* curve of an organic solar cell can be seen in figure 1.6. From such graph a few important performance parameters can be extracted, mainly the open circuit voltage, short circuit current, fill factor, and maximum power. Open circuit voltage (V_{OC}) is the maximum photovoltage the cell can supply and is the voltage for which the current under illumination is zero. Similarly, the current that runs through the cell at zero voltage corresponds to the short circuit current (J_{SC}). Being power the product of current and voltage, the point of the curve where $J \times V$ is maximum, represents the maximum power output (P_{MAX}). Finally, the fill factor (FF) is a way of calculate the quality of the *J-V* characteristic, and is given by the ratio of P_{MAX} and the product
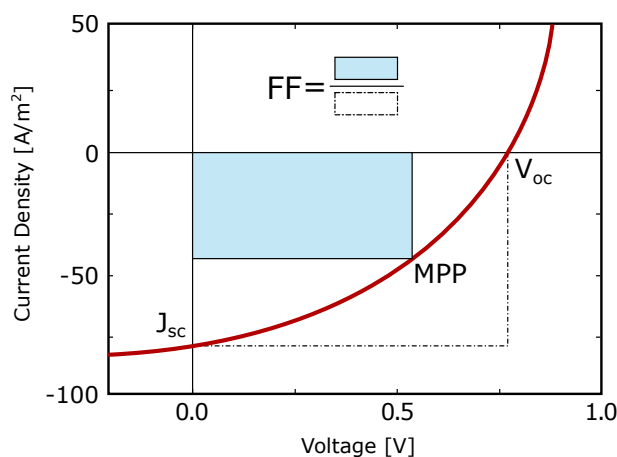
Figure 1.6: *Typical current density-voltage characteristic of an organic bulk-heterojunction solar cell. The characterization parameters J_{SC}, V_{OC}, and FF are indicated. The maximum-power point (M_{PP}) is also shown, where the maximum power P_{MAX} that the solar cell can supply is represented by the filled rectangle.*

of $J_{SC} \times V_{OC}$. This parameters allow us then to determine the power conversion efficiency (PCE), η, of the cell, which is given by the ratio between P_{MAX} and the incident power, P_{IN}:

$$\eta = \frac{P_{MAX}}{P_{IN}} = \frac{J_{SC}V_{OC}FF}{P_{IN}} \tag{1.5}$$

1.3 Perylene Diimides

Perylene-3,4,9,10-tetracarboxylic acid diimide derivatives, also known as perylene diimides (PDIs), are n-type organic semiconductors and common non-fullerene acceptors used in OPVs. PDIs generally show high thermal, chemical, and light stabilities, good electron-accepting abilities due to the well placed LUMO energy, and excellent electron mobilities [21–24]. Compared to fullerenes, PDIs show a strong and broad absorption in the visible spectral region and their optoelectronic properties are easily tuned by tailoring the substituents on the imide-N, bay, and/or non-bay positions (see figure 1.7). This makes PDIs promising candidates to replace fullerenes, however they have been falling short in terms of performance. Traditional PDI derivatives show over-strong aggregation, leading to formation of large (tens to hundreds of nanometers) crystalline aggregate domains. In these structures, excitons decay into intermolecular states and the well-ordered PDI domains act as charge traps, severely limiting exciton diffusion/separation efficiencies and further the PCE of the devices [25]. To avoid over aggregation and PDI columnar stacking, non-planar PDI derivatives such as dimers [26] or star-shaped structures [27] are beginning to be used, which have demonstrated a certain increase in PCEs. However, much remains to be known about PDIs and their derivatives.
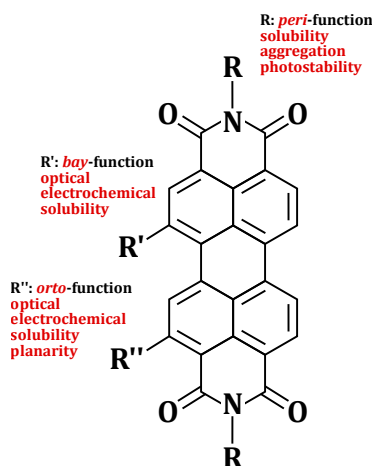
Figure 1.7: *Illustration of the chemical structure of the PDI base structure and the possible positions for the tuning of its properties.*

Materials and Methods

The work conducted in this dissertation involved the synthesis of different active layer solutions and fabrication and characterization of various organic solar cells. Following substrate cleaning, spin coating of the relevant blends and deposition of electrodes was done. Active layer films and final devices were morphologically and electrically characterized, respectively. This chapter summarizes relevant materials, techniques and software programs used.

2.1 Substrate Cleaning

The devices were fabricated on 3×3 mm, pre-patterned ITO coated glass substrates (OPVs and hole-only) and non-coated ones (electron-only). The substrates were treated/cleaned with a sequential process of scrubbing with water and neutral soap for 6 minutes, 5 minute long ultrasonic baths (both in acetone and isopropanol) and 25 minutes of UV-Ozone. The entire above mentioned cleaning process was done in air, inside a ISO class 6 cleanroom.

2.2 Solution synthesis

2.2.1 Solution Solvents

Commercial Chlorobenzene (CB) and Chloroform (CF) were obtained from Sigma Aldrich. Their chemical structure can be found in the Appendix, auxiliary figure A1.

2.2.2 Donor and acceptor materials

Commercial regioregular poly(3-hexylthiophene-2,5-diyl) (P3HT) was purchased from Solarmer Materials Inc. Commercial Perylene Diimide (PDI) and Phenyl-C61-butyric acid methyl ester ($PC_{61}BM$) were purchased from Sigma-Aldrich Co. LLC, and the PDI derivatives were supplied by the group of Prof. Müllen, from the MPIP. For convenience, these materials will be from now on referred to as PDI-1 (commercial PDI), PDI-2, PDI-3 and PDI-4. The structure of the aforementioned materials can be found in auxiliary figure A2, with the exception of the PDI derivatives due to confidentiality reasons.

2.2.3 Active Layer Solution (P3HT:PDI and P3HT:PCBM)

For preparation of the active layer, P3HT and the relevant PDI derivative were dissolved in CF at different concentrations and ratios, and then both heated and stirred overnight in a nitrogen filled glovebox (with typical O_2 and H_2O levels below 1 ppm). Solutions were then filtered through a PTFE syringe filter. P3HT:PCBM solutions were prepared in an identical fashion, in this case with a ratio of 1:1 and concentration of 30 mgml^{-1}.

2.3 Device fabrication

2.3.1 Material deposition

The OPVs and HO devices require a PEDOT:PSS layer on top of the ITO for better wetting of subsequent polymer layers, better smoothness and energy level matching. The spin coating of this layer was also done inside the clean room, using a Lab spin 6/8 spin coater, from Suss MicroTech GmbH. Immediately after the UV-Ozone treatment, PEDOT:PSS (Clevios P VP

Al4083) was filtered with a 0.45 µm filter directly onto the substrate and, unless otherwise noted, a standardized program was used to spin coat at 2500 rpm, in room temperature. After spin coating of this layer, the samples were annealed/dried in the oven at 140°C for 10 minutes. As for the active layers itself, right after filtering the prepared solution, spin-coating of the active layers was done inside a nitrogen filled glovebox.

2.3.2 Contact evaporation

Top and bottom metal contacts were deposited through a specific shadow mask for each of the two layers, which results in four active areas with 1×10^{-5} m², 1.5×10^{-5} m², 3.75×10^{-5} m² and 9.95×10^{-5} m². The device structure and sample layout of the single carrier devices and OPVs are depicted in auxiliary figure A3. This process was conducted in a vacuum evaporator system (from Vactec LLC, auxiliary figure A4) under a typical pressure around 5×10^{-7} mbar. During the evaporation process the sample were constantly rotated for improved layer uniformity. In electron-only (EO) devices, an aluminum (Al) anode layer, with a thickness of 30 nm is evaporated prior to spin-coating of the active layer, then left in outside air for 10 minutes to form an oxide layer of about 2-3 nm. Depending on the device (OPV, HO or EO), different top contacts were used. These consisted of either Barium/Aluminum (Ba/Al), Lithium Fluoride/Aluminum (LiF/Al) or Gold (Au). The Ba layer of 5 nm was deposited using a manual program at an initial rate of about 0.5 nm/s gradually moving up to 1 nm/s. Regarding the LiF layer, a total thickness of 1 nm was also deposited via a manual program, with a rate of about 0.1 to 0.2 nm/s. Aluminum and gold were deposited with an automatic program, both for a thickness of 100 nm. The programs starts with a low rate and ends with a rate of 1 nm/s.

2.3.3 Thermal Annealing

Thermal annealing of the devices, was performed on a hot plate inside a glovebox, either before top contact evaporation (pre annealing) or after (post annealing).

2.4 Device characterization

2.4.1 Atomic force microscopy (AFM)

Surface morphology characterization of the PDI as-spun and annealed films, was performed by Atomic Force Microscopy (Veeco Digital Instruments, DI 3100 Cl, standard tip 300 KHz).

2.4.2 Electrical characterization

Two different setups were used for electrical measurements of the devices fabricated. Current-voltage (*I-V*) curves, external quantum efficiency (EQE) and density filter measurements were done in nitrogen ambient using a Glovescan system from ECN. The other setup consists of a prototype system (see auxiliary figure A5) put together by technicians from MPIP, where is possible to measure *I-V* curves while controlling the temperature via liquid nitrogen. This way, is possible to perform temperature scans on the single carrier devices. To be noted that all measurements, for stability and degradation reasons, were done in the same day of fabrication.

2.4.3 Simulation

To model the measured *J-V* characteristics of the fabricated single carrier devices, two computer programs were used. The first only uses the Mott-Gurney's law for space-charge limited current in a trap free intrinsic semiconductor (equation 1.1). The second is a pascal computer software, SIMsalabim 2.7, where Pasveer's unified description of charge carrier mobility (equation 1.3a, which takes into account temperature, carrier density and electric field) and other models are available to fit the experimental data.

Results and Discussion

This chapter presents the different experiments made and the discussion of the associated results. These will be divided into three parts: in section 3.1, P3HT:PCBM solar cells are fabricated and characterized to serve as reference cell; chapter 3.2 addresses the main focus of the work of charge carrier transport properties of a commercial PDI acceptor material in single carrier devices and solar cells based; in chapter 3.3, novel PDI derivatives, supplied by the group of Prof. Müllen, from the MPIP, are also tested in single carrier devices.

3.1   P3HT:PCBM system

P3HT/PCBM BHJ solar cells were fabricated to serve as a reference in our working conditions (equipment, material batches, processing methods, etc.). Literature results for optimized P3HT/PCBM systems, without any additive or additional layers, report PCE values of around 2-4 % [28, 29].

Solar cells were made, using a solution blend of P3HT:PCBM (1:1 wt/wt) in chloroform with a concentration of 30 mgml^{-1}. PEDOT:PSS and the active layer solution were spin coated at 500 rpm and 3000 rpm for a layer thickness of 60 nm and 300 nm, respectively. The devices were topped off with a LiF/Al cathode. The measured *J-V* characteristics under light and in dark are shown in figures 3.1a, 3.1b. The cells were measured with an input power P_{IN} of about 890 W/m². The P3HT:PCBM solar cells had an maximum values for V_{OC} and J_{SC} of 0.56 V and 58.08 A/m², respectively, resulting in a FF of 49.74 % and a maximum PCE of 1.815 % (see table 3.1 for full average metrics). These results seem to fall short in terms of performance compared to above mentioned optimized systems of P3HT:PCBM cells from literature, although to confirm their exact active area values would have to be known and considered.

One of the main performance-limiting mechanisms in many organic bulk-heterojunction solar cells is non-geminate recombination of separated charge carriers. Thus, understanding the recombination mechanisms of separated charge carriers is crucial to design strategies to reduce non-geminate recombination [30]. A particularly important indicator of the recombination mechanism is the so-called ideality factor. An ideality factor of 1 indicates a bimolecular recombination, whereas an ideality factor of 2 implies that monomolecular recombination (Shockley-Read-Hall recombination, i.e. trap-assisted recombination) is dominant [31]. One way to obtain the ideality factor is by calculating the slope of the exponential regime for the dark *J-V* characteristics at forward bias, and that can be expressed as [32]

$$\eta = \left(\frac{kT}{q} \frac{\partial ln J_d}{\partial V_{bias}} \right)^{-1}$$

(3.1)

where kT is the thermal energy, J_d is the dark current and V_{bias} the applied voltage. In P3HT:PCBM solar cells, the dark *J-V* characteristics under forward bias are expected to show typical diode behavior: leakage contribution at low voltages, exponential regime at intermediate voltages and space charge limited current after the built-in voltage (V_{bi}). Unfortunately the *J-V* profile of the dark current under forward bias, of the fabricated P3HT:PCBM OPVs, did not allow for a calculation through this method.

An alternative way to determine the ideality factor is to use the light intensity and V_{OC} instead of the current and the external voltage in the dark. At open circuit, the integrated generation and recombination rates must be identical to ensure zero net current flow. At this voltage, all

(a)

(b)

(c)
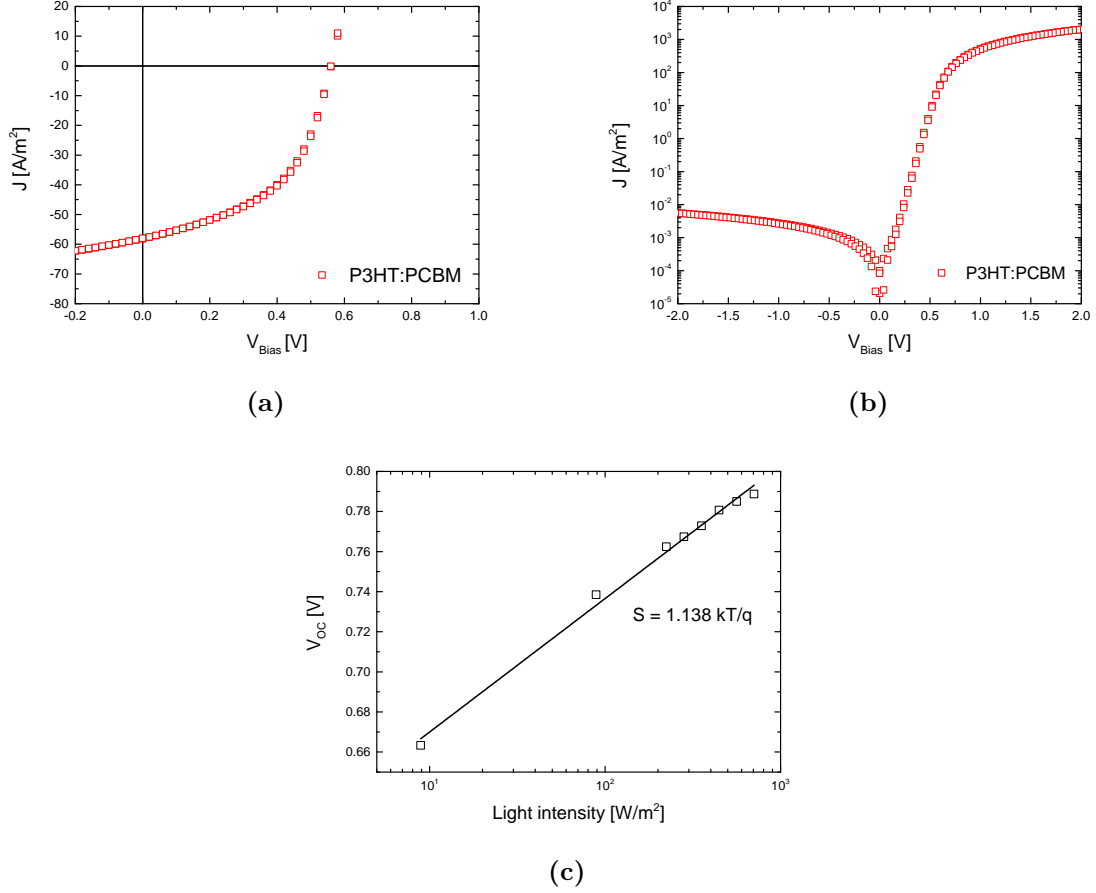
Figure 3.1: *J-V characteristics of P3HT:PCBM (1:1 wt/wt) solar cells (a) under light and (b) in dark. (c) V_{OC} vs light intensity of the same solar cells.*

Table 3.1: *Average metrics of the P3HT:PCBM (1:1 wt/wt) solar cells. For the study of this system 3 devices were characterized.*

Device system	Thickness [nm]	$\mathbf{V_{OC}}$ [V]	$\mathbf{J_{SC}}$ [A/m²]	FF [%]	PCE [%]
P3HT:PCBM (1:1)	300	0.56 ±0.01	38.96 ±19.12	51.76 ±2.67	1.26 ±0.55

photogenerated charge carriers recombine. This implies that the open-circuit voltage is limited by the amount of recombination that is present in the device. Therefore, a reduction in the recombination strength would lead to a higher open-circuit voltage. Because the generation rate is proportional to the light intensity, the dependence of the V_{OC} on the light intensity can be a more reliable and sensitive method to determine the recombination mechanisms present in the solar cells [33], compared to calculating it through the dark current. The open-circuit voltage can be expressed as

$$V_{OC} = \frac{E_{gap}}{q} - \frac{kT}{q} ln \left(\frac{(k_R)N_c^2}{G} \right) \tag{3.2}$$

with E_{gap} the energy gap between the HOMO of the acceptor and the LUMO of the donor, k_R the bimolecular recombination coefficient, N_c^2 the density of states, and G the generation rate of excitons.

Plotting the V_{OC} values as a function of the natural logarithm of light intensity, a slope kT/q of

roughly 1.2 is obtained, as depicted in figure 3.1c. This can be interpreted as an ideality factor of ∼1.2, pointing to the absence of deep traps and to recombination being mostly bimolecular. However, fitting a straight line to a V_{OC} vs light intensity plot, resulting in a slope of one could be from averaging over different recombination mechanisms. At the same time, ideality factors from dark currents that often are much larger than one, are no proof of trap-assisted recombination as it can be caused by resistive effects [33]. Therefore, in order to get a more precise ideality factor, further experiments have to be done, where the the latter is retrieved from the light output of the solar cell (when stressed).

3.2 Donor:PDI systems

3.2.1 AFM characterization of PDI films

As mentioned previously, several reports on PDI-based OPV blend films have underlined the detrimental effect of PDI aggregates that could act as charge traps or as stabilization sites where the PDI excitons convert to PDI excimers and limit charge photogeneration efficiency. The dimerization of PDI was suggested as the means to impose steric hindrance between adjacent PDI monomers and to impede PDI π-π stacking. However it is not yet clear whether in the solid state of these systems the formation of PDI aggregates is being actually suppressed [34]. Efficiency is dictated by the electronic coupling between adjacent PDI aggregates and by the proper orientation of these in respect to the charge-carrier collecting electrodes. So it can be that PDI aggregation takes place also in the efficient composites of the PDI dimers but that these aggregates facilitate charge photogeneration and transport due to a favorable structural motif. On the other hand, non-planar PDI derivatives have the disadvantage of requiring many reaction steps which makes their synthesis process more expensive and complicated. Therefore, it is important to address the process of PDI aggregation in OPV polymeric composites in order to provide the guidelines for the synthesis of next-generation PDI n-type components.
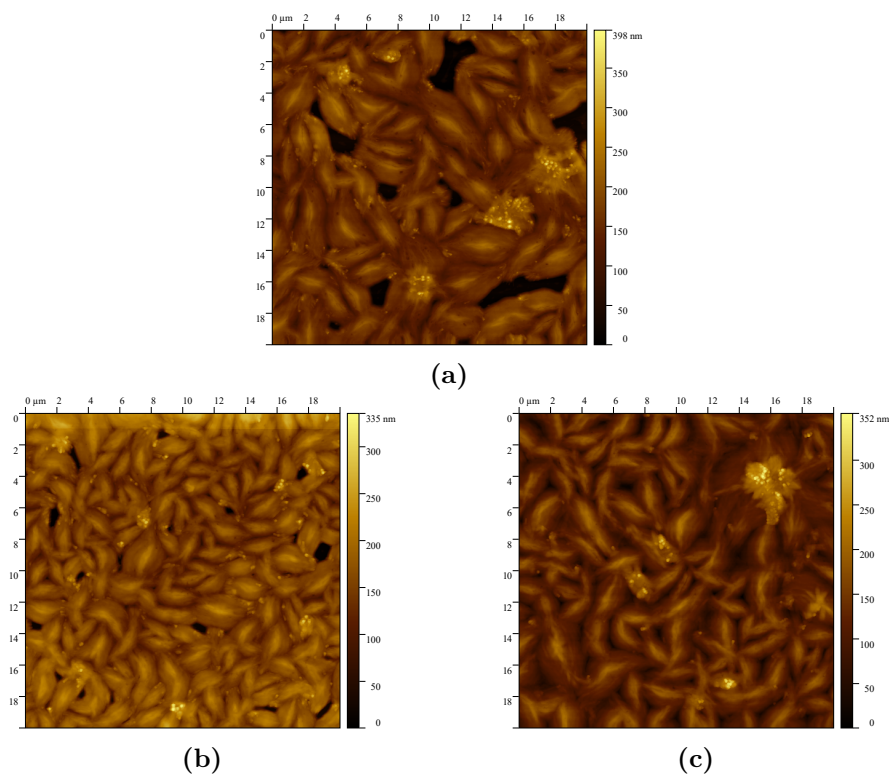
Figure 3.2: *AFM pictures of pristine PDI-1 films annealed for 30 min at (a) 50°C, (b) 60°C and (c) 80°C.*

PDI-1 in chloroform

Figure 3.2 shows the surface topography, measured by AFM, of pristine PDI films cast from chloroform. The films were annealed for 30 min at different temperatures to observe the effect on PDI aggregation. The AFM images of the pristine PDI-1 films, show several micrometer large crystalline structures. Thermal annealing temperatures were not far apart, however there is a slight increase of the PDI-1 crystal size and their packing (increased crystal density). In all cases the domains are clearly separated from each other by distinct grain boundaries which are known to limit the charge carrier transport in thin layers [35].

P3HT:PDI-1 (1:1 wt/wt)

It has been reported that the D/A blend morphology can be controlled by the solvent from which the blend is spin-coated, to try and minimize large-size phase separation and/or enhancing polymer chain packing [36, 37]. Figure 3.3 shows the surface topography, measured by AFM, of films cast from a P3HT:PDI-1 blend in CF and in CB. From figure 3.3a it can be seen a large phase separation between the P3HT and PDI and large PDI-1 crystals is observed for the CB-processed P3HT:PDI-1 (1:1 wt/wt) blend film. The large PDI-1 crystals results in also large P3HT domains in between the PDI-1 crystalline particles. In the case of the P3HT:PDI-1 blend film processed from CF, shown in figure 3.3b, the phase-separation and PDI crystal formation is significantly reduced. This difference is due to the fact that CB has a higher boiling point than CF, which results in a slower evaporation rate compared to that of CF. Thermal annealing at 100°C of the films processed from CF (figure 3.3b), leads to the appearance of ribbon-like elongated features.

(a)

(b)

(c)

(d)
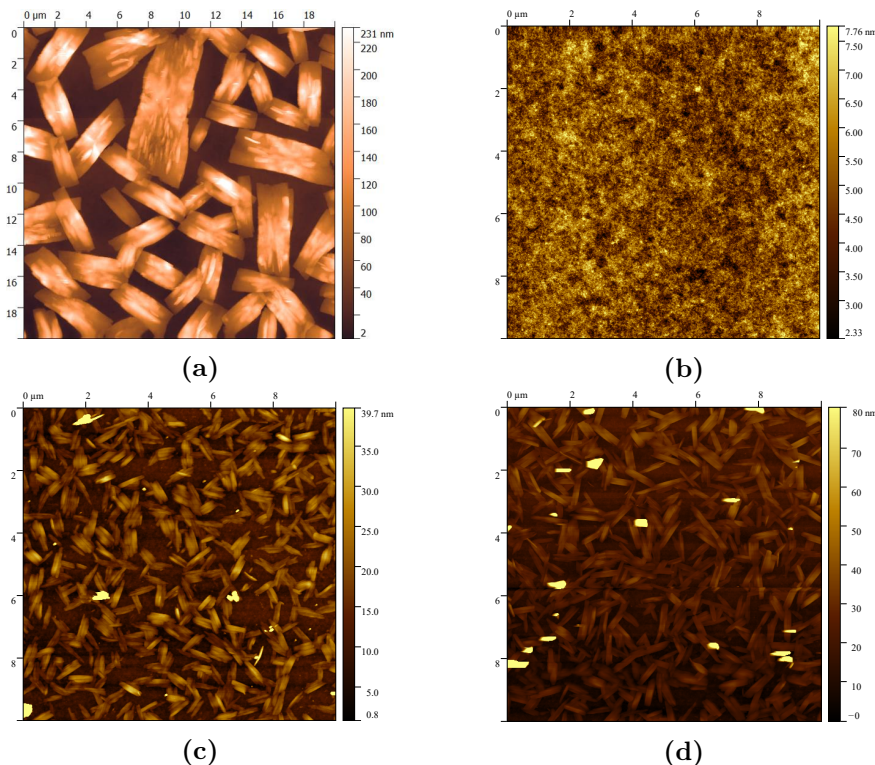
Figure 3.3: *AFM height images of P3HT:PDI-1 blend films with different PDI fraction, cast from CB and CF, non-annealed and annealed. (a) As-spun P3HT:PDI-1 (1:1 wt/wt) film cast from CB; (b) As-spun P3HT:PDI-1 (1:1 wt/wt) film cast from CF; Annealed (10 minutes at 100°C) P3HT:PDI-1 (1:1 wt/wt) film cast from CF; and annealed (10 minutes at 100°C) P3HT:PDI-1 (1:4 wt/wt) film cast from CF.*

The change of PDI fraction apparently yields no big change in the microstructure of the film. Increasing the PDI-1 content in the blend to 1:4 (P3HT:PDI-1) results in a slight bigger density of PDI-1 crystals but its average size stays virtually the same (figure 3.3d).

Cross-sectional scanning electron microscopy (CS-SEM) characterization of the P3HT:PDI-1 films would be needed to assess vertical phase separation and the creation of the necessary network for the charge carrier percolation pathways.

3.2.2 MEH-PPV:PDI-1

Solar cells and electron-only devices were fabricated using MEH-PPV as donor material. PE-DOT:PSS and an active blend solution of MEH-PPV:PDI-1 (1:4 wt/wt) in chloroform (16.67 mgml^{-1}), were both spin coated at 1200 rpm, for a layer thickness of 50 nm and 260 nm, respectively. Devices were toped off with a Ba/Al cathode and post annealed for 10 min at 110°C. The solar cells were measured with a P_{IN} of about 890 W/m². The measured *J-V* characteristics under light and in dark are shown in figure 3.4, for both non-annealed and annealed devices.

Upon annealing, the solar cells show an increase of J_{SC}, of roughly 1.25 fold, while V_{OC} remained unchanged at ∼0.79 V, resulting in an average PCE of 0.022 %. Not annealed devices had an average PCE of 0.017 %. The device metrics are summarized in table 3.2. As can be observed in figure 3.4b, the dark *J-V* characteristics show typical diode behavior for forward bias and by using equation 3.1, we obtain an ideality factor of ∼2 and ∼1.8 from the dark current, of the non-annealed and annealed devices, respectively. In contrast, the slope S of the V_{OC} vs light intensity characteristics of the non-annealed solar cells gives an ideality factor of roughly 1.1 (see figure A6). As mentioned before, is difficult to draw conclusive observations from ideality factors retrieved from the solar cells current, however the results from V_{OC} dependence on light intensity are more reliable and point to a predominant bimolecular recombination mechanism.

(a)   **(b)**
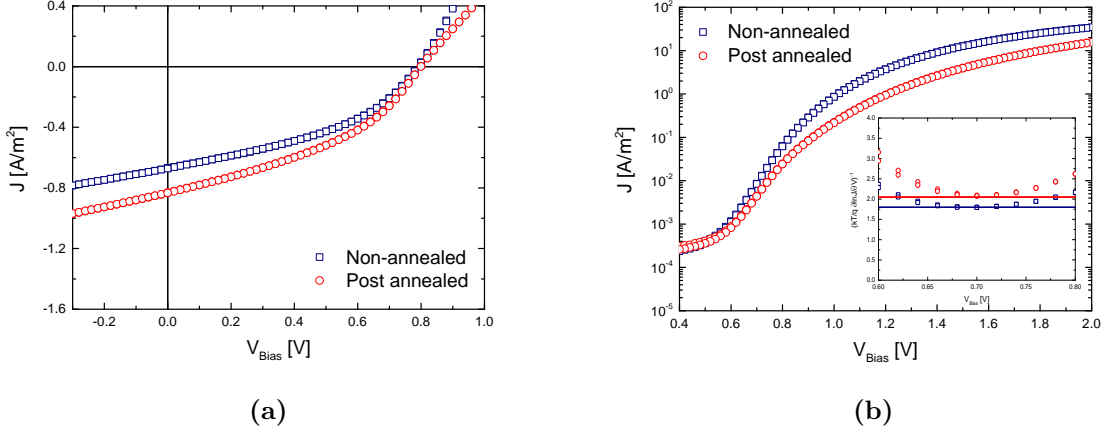
Figure 3.4: *J-V characteristics for the non-annealed (blue) and post annealed (red) MEH-PPV:PDI-1 (1:4 wt/wt) devices (a) under light and (b) in dark. The inset of (b) shows the differential plot of the data according to equation 3.1.*

Table 3.2: *Average metrics of the MEH-PPV:PDI-1 (1:4 wt/wt) non-annealed and post annealed solar cells, with a active layer thickness of ∼260nm. For the study of this layer system 3 devices were characterized.*

MEH-PPV:PDI-1 (1:4)	V_{OC} [V]	J_{SC} [A/m^2]	FF [%]	PCE [%]
Non-annealed	0.78 ±0.01	0.49 ±0.18	39.73 ±1.97	0.017 ±0.007
Post annealed	0.80 ±0.01	0.62 ±0.22	39.60 ±0.89	0.022 ±0.007

Electron-only devices have been fabricated. Measuring their *J-V* characteristic and then fitting the data with the SCLC model, the parameters of the electron mobility can be determined. Repeating the process using the drift-diffusion model from Pasveer, for different temperatures, the temperature dependency of the mobility can be found, as well as an approximation of the site spacing and energetic disorder of the active blend. The electron-only currents, before and after post annealing, are plotted as a function of the applied voltage, and are presented in figure 3.5a. There is a slight different injection behavior from each electrode, however, for the voltage range used, both seem to show ohmic currents. Electron injection appears to be higher from (Al_2O_3) as compared to injection from the Ba/Al electrode. In a log-log plot of current density vs voltage, an ohmic behavior results in a slope of 1, while SCLC gives a slope of 2. As observed in figure 3.5b a slope of approximately 1 is observable, confirming therefore, an ohmic regime for the range of applied fields. Ohmic currents in undoped semiconductors are often a result of the diffusion of charge carriers present in the metal contacts [38]. However this effect should not be noticeable for such a thick active layer (260 nm), which leads to believe that we have unwanted doping. Upon thermal annealing, current density of the EO device decreases slightly, probably due to the removal of the just mentioned dopants.

A current that follows Ohm's law is described by the following expression

$$J = qp_0\mu\frac{V}{L} \tag{3.3}$$

where p_0 is the background charge carrier density. However, looking at the temperature scan in figure 3.6, the *J-V* characteristics of the EO device show a clear and significant temperature dependency. To verify the presence of a SCLC in the device, re-measuring of the *J-V* charac-

(a)   **(b)**
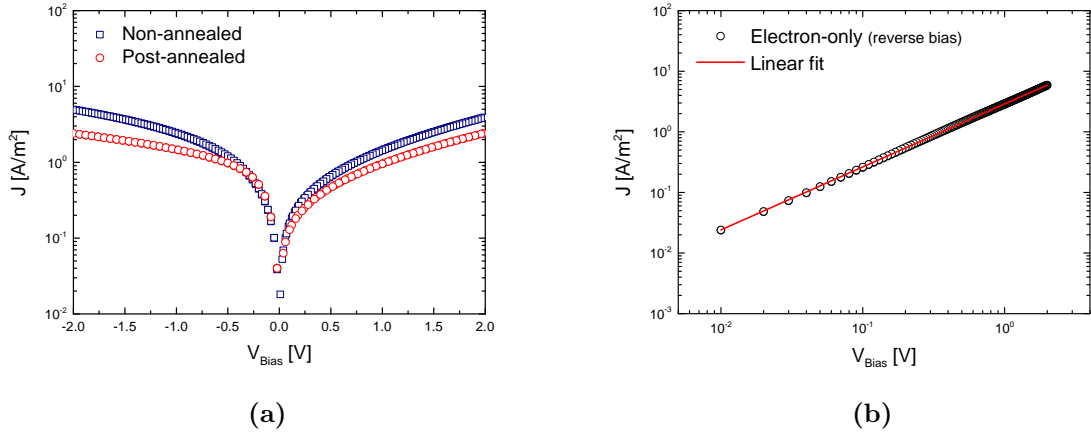
Figure 3.5: *(a) Experimental J-V characteristics (symbols) of a non-annealed (blue) and annealed (red) MEH-PPV:PDI-1 (1:4 wt/wt) EO device and (b) again of a non-annealed device at reverse bias. The solid line is an automatic linear fit to the experimental data with slope 1.*

teristics at higher voltage values is required. Once the electron mobility is determined we can then predict the charge carrier concentration through equation 3.3.
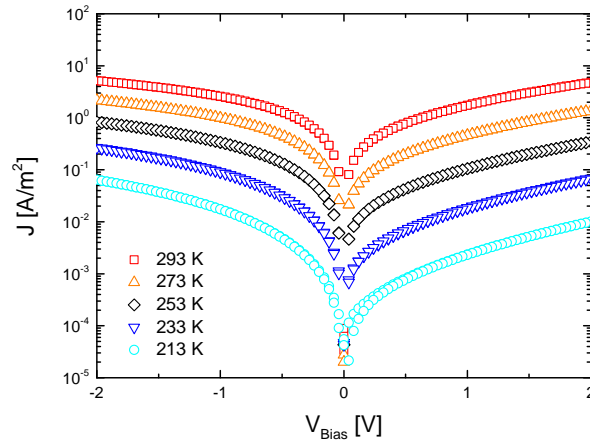
Figure 3.6: *Temperature-dependent J-V characteristics of a non-annealed EO device with a MEH-PPV:PDI-1 (1:4 wt/wt) active layer system.*

3.2.3 P3HT:PDI-1

PDI-1 has been rather used previously in other literature works, however much remains to be known about its electronic properties, namely charge transport, in PDI-based OPVs. To study the behavior of PDI when blended with P3HT, devices with an active layer of P3HT:PDI-1 have been fabricated. Solar cells and EO devices were made, using a solution blend of P3HT:PDI-1 (1:1 wt/wt) in chloroform with a concentration of 10 mgml^{-1}. PEDOT:PSS and the active blend solution were both spin coated at 1200 rpm, for a layer thickness of 50 nm and 120 nm, respectively. The OPVs were toped off with a LiF/Al cathode, while for EO devices Ba/Al was used. Four sequential steps of 5 minutes of annealing at 120°C (total of 20 minutes) were performed on the completed devices, and temperature dependent *J-V* characteristics were measured after each annealing step. In figure 3.7a, the *J-V* characteristics after the first three different annealing steps is shown. A significant current asymmetry across the EO device layer is found for both non-annealed and post annealed devices. Looking at the reverse bias side, i.e. Al$_2$O$_3$, there is a

15

(a)

(b)
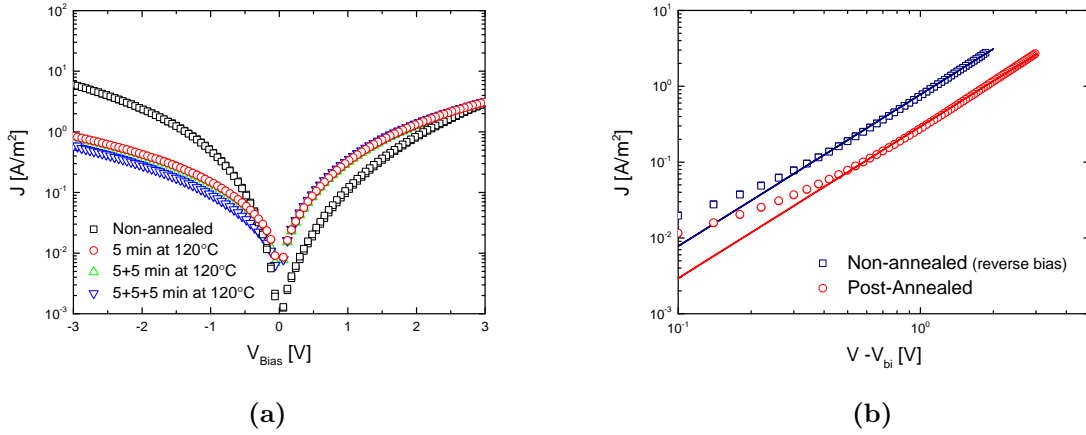
Figure 3.7: *(a) Experimental J-V characteristics (symbols) before and after three consecutive annealing steps of 5 min at 120°C of a P3HT:PDI-1 (1:1 wt/wt) EO device, with a layer thickness of about 120 nm. (b) Fitting (solid lines) of the non-annealed (blue)(reverse bias) and post annealed (red) EO devices, calculated using equation 1.1. For the non annealed device a V_{bi} of 0.12 V was used.*

significant reduction in current density upon the first 5 minutes of annealing. A possible reason is that in the non-annealed devices, there are already present impurities (i.e. positive ions) that will contribute in the charge transport and/or that the thin oxide layer does not provide a big enough barrier to fully block hole injection from the Al contact. When the device is annealed, interfacial states are removed and structural rearrangement takes place at the interface. On the other hand, electron injection from from the Ba/Al side increases upon annealing (at lower applied fields) and, overall, a more balanced electron current across the whole device is obtained. For all further annealing steps, the measured current densities were practically the same, only showing a minimal decrease on the Al_2O_3 side.

In figure 3.7b, the electron-only currents are plotted as a function of the applied voltage (corrected for the built-in voltage V_{bi}), and fitted accordingly. These currents can be well described by equation 1.1 for SCLC, exhibiting a quadratic dependency on voltage. The electron mobility values obtained from such model, for the non-annealed (at reverse bias) and annealed (at forward bias) devices, were 4.5 x 10^{-11} m²/Vs and 1.7 x 10^{-11} m²/Vs, respectively. However, this model doesn't take into account charge carrier density and electric field variations. Therefore, without measuring the *J-V* characteristics and fitting them for a range of different layer thicknesses (minimum 3), there is no way to confirm that the currents are fully bulk limited and the presented electron mobilities, which can only be considered an approximation and are predicted to be considerably lower.

Figure 3.8 shows the temperature dependent *J-V* characteristics of an EO device, before and after post annealing. The best fit of the experimental data was obtained using the values expressed in table 3.3. The mobility retrieved from the unified description of Pasveer, was 3.17 x 10^{-13} m²/Vs and 3.67 x 10^{-13} m²/Vs, respectively for non-annealed and post annealed devices. For the full range of voltage and temperatures used, the modeling describes very well the experimental *J-V* characteristics, although regarding the post annealed EO devices, the current tends to be more ohmic than space-charge-limited at lower applied fields. This phenomenon has been described and is related to the movement of the virtual cathode (the point of zero electric field) as a function of voltage [39]. Nevertheless, the good agreement of the current-voltage characteristics with eq.1.1 in the low field regime and the accurate description of the temperature dependent currents with the drift-diffusion model are strong indications that the electron transport is essentially trap free.

Figure 3.9, shows the electron and hole current densities of non-annealed P3HT:PDI-1 (1:1 wt/wt) EO and HO devices with a layer thickness of 210 nm. Again they exhibit a quadratic

Table 3.3: *Fit parameters used for modelling the temperature-dependent J-V characteristics of a non-annealed and annealed P3HT:PDI-1 (1:1 wt/wt) EO device with a layer thickness of 120 nm.*

Device	μ_0 (295 K)	Mobility pre-factor	Width of Gaussian, σ	Site spacing, a	Φ left/right	V_{bi}
Non-annealed	3.17 x 10⁻¹³ m²/Vs	1600	0.158 eV	1.7 nm	0/3 eV	0.12 V
Post annealed	3.64 x 10⁻¹³ m²/Vs	500	0.148 eV	1.2 nm	0/3 eV	0 V

dependence on voltage and can be well fitted using equation 1.1. We observe a difference of about two orders of magnitude between the electron and the hole current. This is evidence of a pronounced unbalanced charge transport and that holes are clearly the dominant charge carrier in the P3HT:PDI-1 (1:1 wt/wt) blend.

The *J-V* characteristics under light and dark of a non-annealed and post annealed P3HT:PDI-1 (1:1 wt/wt) solar cell can be seen in figure 3.10. These devices were measured with a P_{IN} of about 1460 W/m². The summarized solar cell metrics are found in table 3.4.

The non-annealed devices exhibit a leakage current regime at low applied forward bias which is not visible anymore in the post annealed ones. This is most probably due to the above mentioned removal of an interfacial barrier (from structural arrangement or presence of interfacial states) with the contacts, upon thermal treatment. However at the same time, this causes saturation current at reverse bias to increase. This reducing of interfacial barrier can also be visible in the decrease of V_{OC} in the *J-V* characteristics under illumination, as observed in figure 3.10a. Here we can see that the J_{SC} of the solar cells is improved by roughly 6.5 fold, while V_{OC} decreased by 1.5 fold. Considering that the electron-mobility decreases with annealing, the performance improvement (due to a higher J_{SC}) of the OPVs, could be associated to the more balanced electron current density (as a result from improved lateral phase separation) removal of an interfacial barrier that promotes charge collection and/or even hypothetically to an increase of the hole mobility upon annealing. Measuring of the *J-V* characteristics of an annealed HO device would be needed to verify this last sugestion. The average fill factor values for not annealed and annealed P3HT:PDI (1:1 wt/wt) solar cells, are 33 % and 28 %, respectively. These low FFs can be mainly explained by the large difference in charge carrier mobilities (i.e. unbalanced transport) (evidenced in figure 3.9), which causes accumulation of space charges and increased recombination [20, 40–42].

As depicted in figure 3.10c, the slope S of the V_{OC} vs light-intensity characteristics equals 0.9 and 2 for the non-annealed and post annealed devices. This can be interpreted as ideality factors of

(a)   (b)
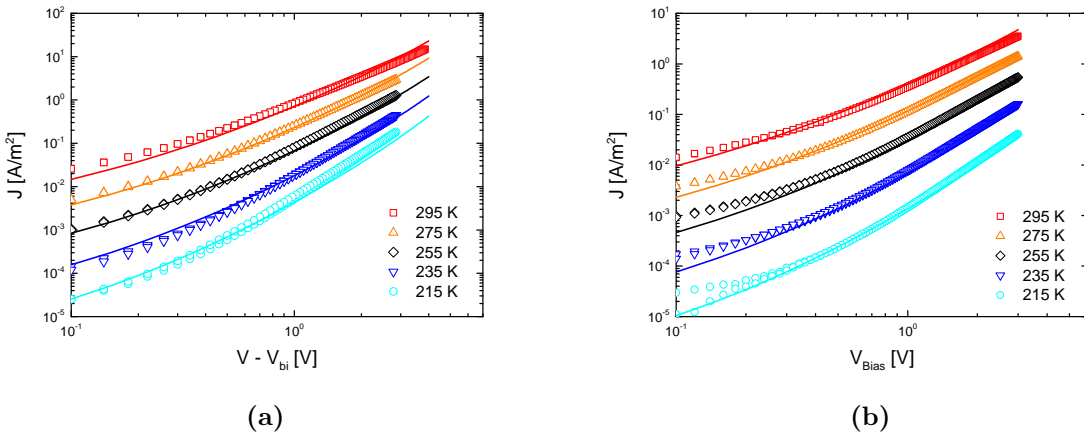
Figure 3.8: *Temperature dependent experimental J-V characteristics (symbols) of P3HT:PDI-1 (1:1 wt/wt) (a) non-annealed and (b) post annealed EO devices. The solid lines are fits to the experimental data, obtained with Pasveer's model (eq.1.3).*

Table 3.4: *Average metrics of the P3HT:PDI-1 (1:1 wt/wt) non-annealed and annealed devices, with a layer thickness of ∼120 nm. For the study of this system 4 devices were characterized.*

P3HT:PDI-1 (1:1) with LiF/Al	V_{OC} [V]	J_{SC} [A/m²]	FF [%]	PCE [%]
Non-annealed	0.521 ±0.10	1.04 ±0.14	32.99 ±4.64	0.012 ±0.005
Post Annealed	0.350 ±0.01	6.07 ±2.12	28.16 ±1.00	0.041 ±0.016

unity and 2, indicating that in non-annealed solar cells recombination is trap-assisted (i.e. SHR, band to band recombination), associated to the just above mentioned pronounced unbalanced transport between electrons and holes which causes recombination to be driven/limited by both carrier types.

P3HT:PDI-1 (1:1 wt/wt) solar cells with a Ba/Al cathode, have also been made. PEDOT:PSS and the active blend solution were spin coated at 2500 rpm and 1200 rpm resulting in a layer thickness of 40 nm and 80 nm, respectively. Both pre annealing and post annealing of the devices was done, for 15 minutes at 100°C. These devices were measured with a P_{IN} of around 890 W/m². The *J-V* characteristics under light and dark of the non-annealed, pre annealed and

Table 3.5: *Average metrics of the P3HT:PDI-1 (1:1wt/wt) devices with a Ba/Al cathode and an active layer thickness of 80 nm. For the study of the systems 3 devices were characterized.*

P3HT:PDI-1 (1:1) with Ba/Al	V_{OC} [V]	J_{SC} [A/m²]	FF [%]	PCE [%]
Non-annealed	0.44 ±0.04	0.45 ±0.16	27.99 ±0.91	0.006 ±0.003
Pre Annealed	0.26 ±0.03	1.64 ±1.01	30.76 ±4.00	0.015 ±0.01
Post Annealed	0.28 ±0.01	2.52 ±0.60	29.48 ±1.65	0.023 ±0.006

post annealed devices can be seen in figure in 3.11b, as well as a summary of their main figures of merit, in table 3.5. Pre annealed devices show a J_{SC} of 1.643 A/m², significantly lower than 2.519 A/m² of the post annealed ones. On the other hand, both pre annealed and post annealed OPVs, have a similar decrease of V_{OC} of around 1.6 fold, which means that the thermal
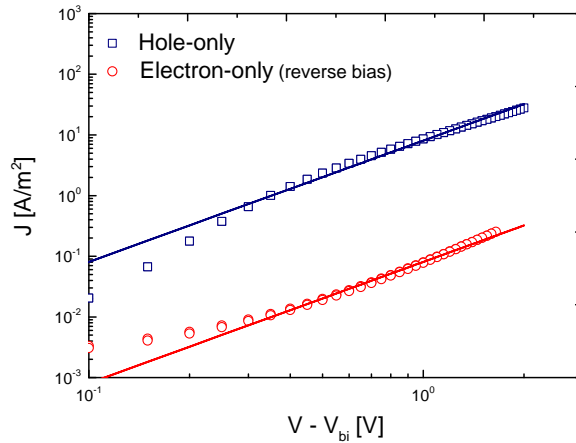
Figure 3.9: *Experimental J-V characteristics (symbols) of a P3HT:PDI-1 (1:1 wt/wt) EO (red)(reverse bias) and HO (blue) device, with layer thickness of ∼210 nm. The solid lines are fits to the experimental data, calculated with eq.1.1 for SCL currents. For the electron-only device, a V_{bi} of 0.35 V was used.*

(a)

(b)

(c)
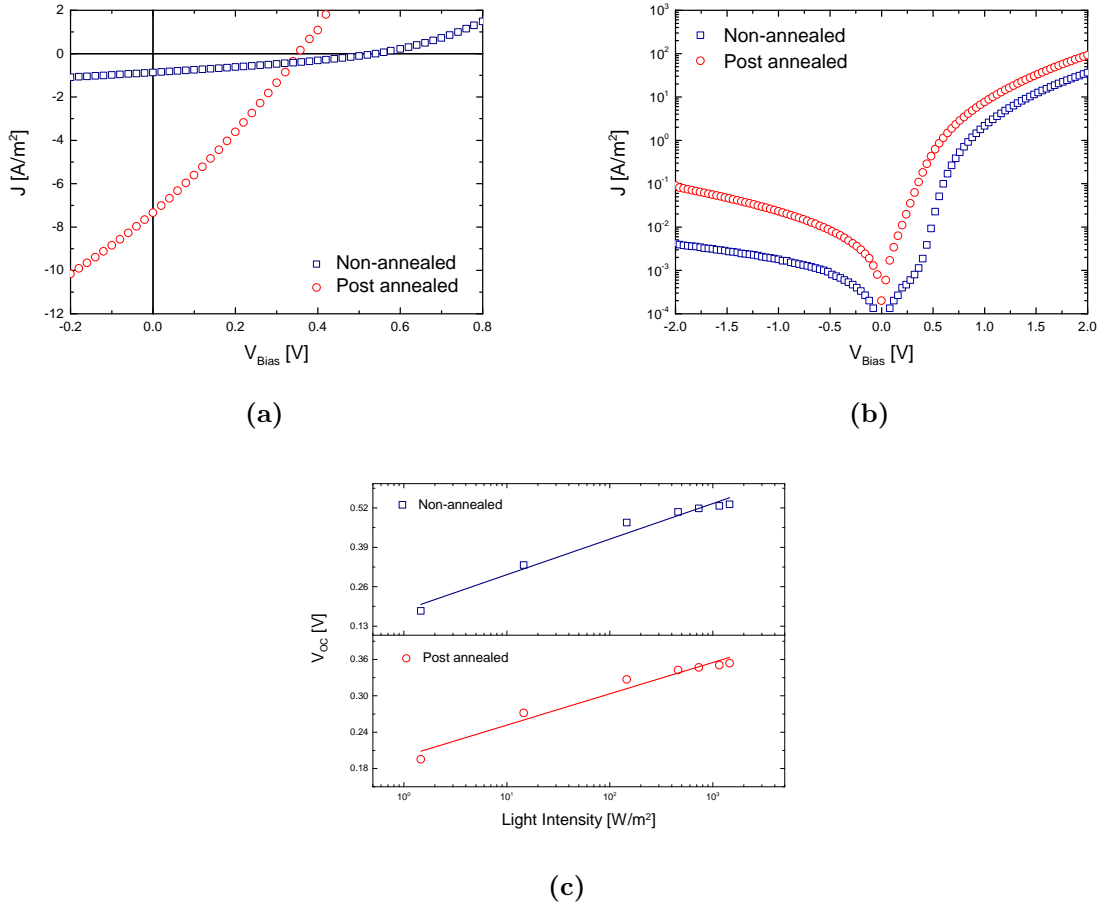
Figure 3.10: *J-V characteristics for the non-annealed (red) and annealed (blue) P3HT:PDI-1 (1:1 wt/wt) devices (a) under light and (b) in dark. (c) Light intensity dependence of $V_{\rm OC}$ for annealed and non-annealed devices.*

annealing of the active layer-cathode interface is not responsible for the $V_{\rm OC}$ loss. This could indicate that annealing of the device results in a less optimal vertical phase separation (where the acceptor material would aggregate towards the interface with the cathode) and/or simply in the degradation of the active layer [43, 44]. Post annealed OPVs yielded the higher PCE values of 0.023 % (0.028 % maximum).

To compare the solar cells made with a LiF/Al cathode and Ba/Al, the *J-V* characteristics for P3HT:PDI-1 (1:1 wt/wt) devices with both cathodes are plotted together in figure 3.12 and their metrics in table 3.6. Solar cell devices with a LiF/Al cathode had higher values across the board (both non-annealed and post annealed). In LiF/Al cathodes, a layer thickness of 1 nm of LiF was used, while 5 nm of Ba were used for the Ba/Al ones. The thinner layer of LiF can facilitates more the collection of charges, which can explain the higher $J_{\rm SC}$ in the solar cells with a LiF/Al cathode. On the other hand LiF has a slightly higher work function of 2.9 eV, compared to the 2.7 eV of Ba. The potential barrier is therefore lower in the solar cells where a LiF/Al cathode was used, causing the $V_{\rm OC}$ to be also lower. Then, as was brought out previously, post annealing has a strong effect on the solar cells that lowers $V_{\rm OC}$ but increases $J_{\rm SC}$ and overall device performance. Increase in current density, however, was higher in the OPVs with LiF/Al as cathode, resulting in an higher average power conversion efficiency.

(a)   **(b)**
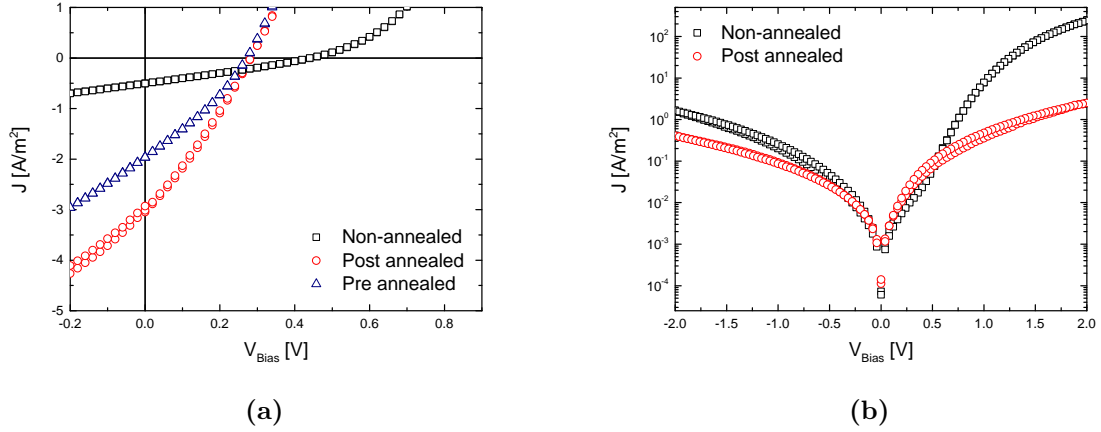
Figure 3.11: *J-V characteristics for the non-annealed (black), pre annealed (blue) and post annealed (red) P3HT:PDI-1 (1:1 wt/wt) solar cells (a) under light and (b) under dark.*
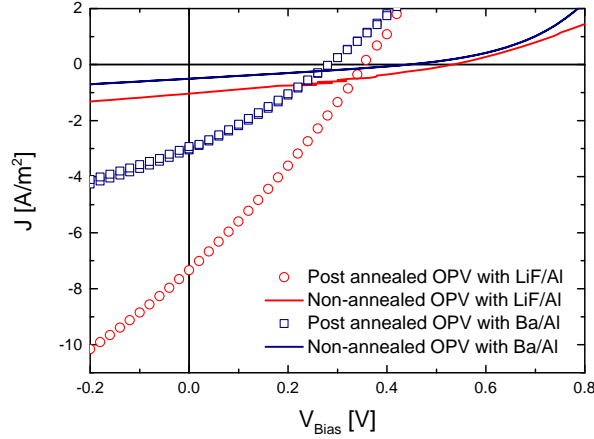
Figure 3.12: *J-V characteristics of P3HT:PDI-1 (1:1 wt/wt) solar cells with a LiF/Al cathode (red) and a Ba/Al cathode (blue), post annealed (symbols) and non-annealed (solid lines).*

Table 3.6: *Average metrics of the non-annealed and annealed P3HT:PDI-1 (1:1 wt/wt) solar cells with a LiF/Al and Ba/Al cathode. For the study of the systems 3-4 devices were characterized.*

Device cathode	Thickness [nm]	Annealing	V_{OC} [V]	J_{SC} [A/m²]	FF [%]	PCE [%]
Ba/Al	80	No	0.44 ±0.04	0.45 ±0.16	27.99 ±0.91	0.006 ±0.003
		Post annealing, 15min at 100°C	0.28 ±0.01	2.52 ±0.60	29.48 ±1.65	0.023 ±0.006
LiF/Al	120	No	0.521 ±0.1	1.04 ±0.14	32.99 ±4.64	0.012 ±0.005
		Post annealing, 5min at 120°C	0.350 ±0.01	6.07 ±2.12	28.16 ±1.00	0.041 ±0.016

P3HT:PDI-1 (1:3 wt/wt)

To investigate the influence of the amount of acceptor material in the blend, solar cells were fabricated with an active blend solution of P3HT:PDI-1 with a 1:3 wt/wt ratio in chloroform. PEDOT:PSS and the active layer solution were spin coated at 2500 rpm and 1500 rpm, for a layer thickness of 40 and 190 nm, respectively. A LiF/Al cathode was then evaporated on top. No annealing of the devices was done and the devices were measured with a P_{IN} of about

(a)   **(b)**
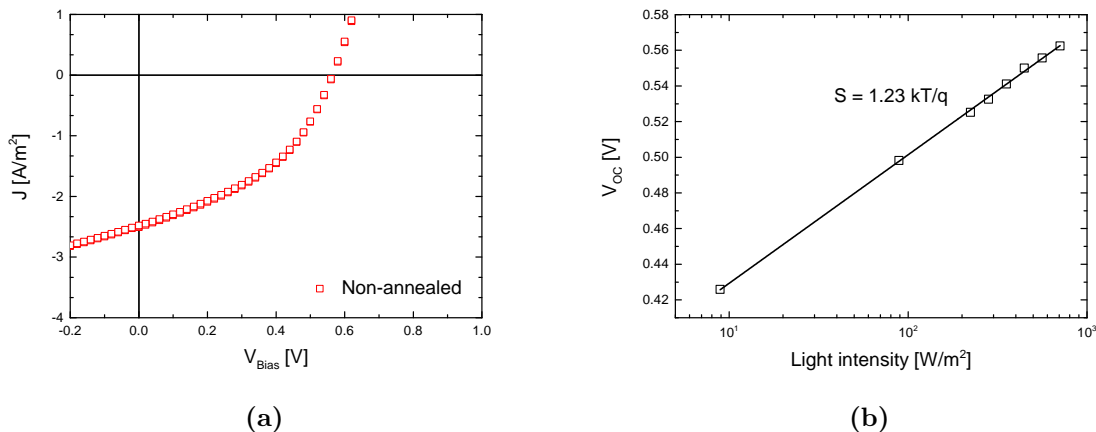
Figure 3.13: *(a) J-V characteristics under light of a P3HT:PDI-1 (1:3 wt/wt) solar cell, with a LiF/Al cathode. (b) V_{OC} of a P3HT:PDI-1 (1:3 wt/wt) solar cell (symbols) as a function of light intensity.*

890 W/m². The *J-V* characteristics, under illumination, of a P3HT:PDI-1 (1:3 wt/wt) active layer solar cell are shown in figure 3.13a.

The obtained maximum values for V_{OC}, J_{SC}, FF and PCE of these solar cells was 0.57 V, 2.5 A/m² and 42.87 % and 0.066 % respectively. The summarized average metric are presented further down in table 3.8. From the V_{OC} vs light intensity characteristics (depicted in figure 3.13b), an ideality factor of ∼1.2 was obtained, which again is indication of a mostly bimolecular recombination process.

Electron-only and hole-only devices with a same P3HT:PDI-1 (1:3 wt/wt) blend were fabricated. A spin speed for the active layer of 1200 rpm gave a thickness of 105 nm. The respective electron- and hole-only currents are plotted in figure 3.14 as a function of applied voltage (corrected for the built-in voltage V_{bi}). The increase of acceptor material (to a ratio of 1:3) results in an increase of electron current of an order of magnitude, compared to EO devices with a P3HT:PDI-1 ratio of 1:1 (wt/wt). As a result there is a much more balanced electron and hole transport across the device layer, and consequently solar cells show a significant improvement in power conversion efficiency. The currents exhibit a quadratic dependence on voltage in the low-field regime and can therefore be described by space-charge-limited transport (eq.1.1). Measurement of temperature dependent *J-V* characteristics of the EO device with a P3HT:PDI-1 (1:3 wt/wt) active layer system was done (see figure A9), however, leakages currents started to be measured for temperature levels below 255 K, which did not allow for a proper respective modelling of the characteristics. Fitting of the temperature dependent *J-V* characteristics and the characteristics for different layer thicknesses is necessary in order to retrieve the electron mobilities in such devices.

P3HT:PDI-1 (1:3 wt/wt) solar cells with a Ba/Al cathode, have also been made. PEDOT:PSS and the active layer solution were spin coated at 2500 rpm and 1200 rpm, for a layer thickness of 40 nm and 105 nm, respectively. Post annealing of the solar cells was done at 110°C for 10 min. Figure 3.15a shows the *J-V* characteristics under illumination, of the non-annealed and annealed OPVs with a P3HT:PDI-1 (1:3 wt/wt) active layer and a Ba/Al cathode. Yet again a drop in V_{OC} and a significant increase in J_{SC} is observable upon annealing. In contrast with the solar cell with LiF/Al as cathode, an ideality factor lower than unity was found, as depicted in the V_{OC} vs light intensity characteristics in figure 3.15b.

(a)   **(b)**
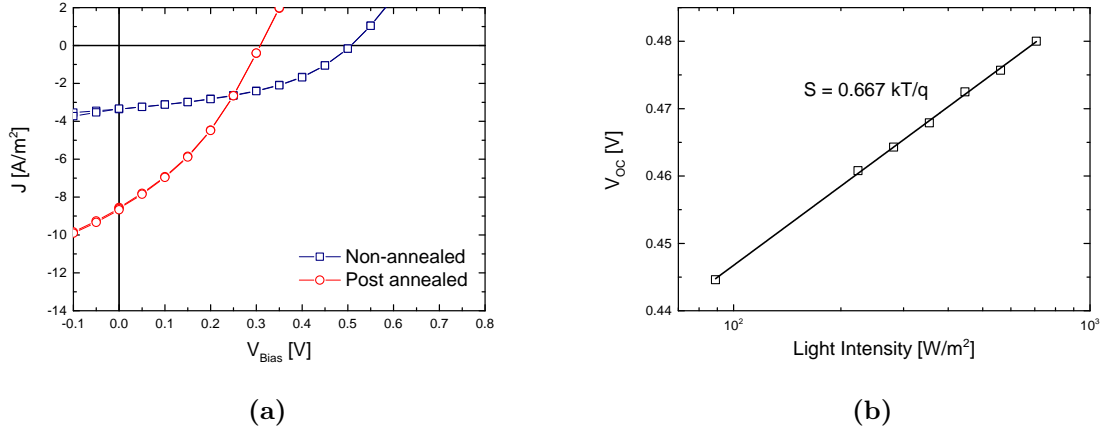
Figure 3.15: *(a) J-V characteristics for P3HT:PDI-1 (1:3 wt/wt) devices with a Ba/Al cathode, before annealing (blue) and post annealed (red). (b) Light intensity dependence of V_{OC} of an non-annealed solar cell.*

Table 3.7: *Average metrics of the P3HT:PDI-1 (1:3 wt/wt) non-annealed and annealed solar cells with a Ba/Al cathode and a layer thickness of 105 nm. For the study of this active layer system 3 devices were characterized.*

P3HT:PDI-1 (1:1) with Ba/Al	V_{OC} [V]	J_{SC} [A/m²]	FF [%]	PCE [%]
Non-annealing	0.49 ±0.05	2.47 ±0.88	40.38 ±3.08	0.055 ±0.028
Post annealed	0.31 ±0.00	6.97 ±1.62	31.17 ±4.10	0.075 ±0.025
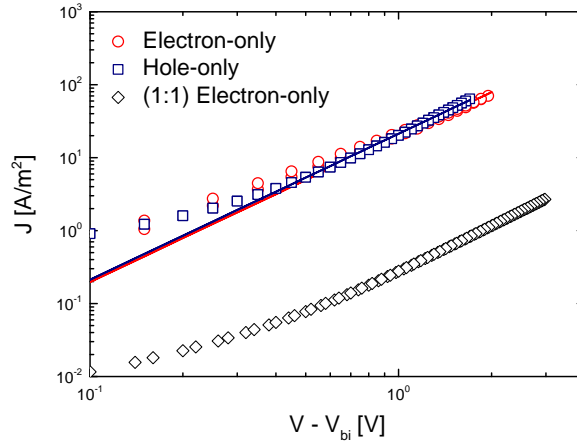
Figure 3.14: *Experimental J-V characteristics (symbols) of a P3HT:PDI-1 (1:3 wt/wt) EO (red) and HO (blue) device, with layer thickness of ∼105 nm. The solid lines are fits to the experimental data, calculated with eq.1.1 for SCL currents. For the hole-only device, a V_{bi} of 0.3 V was used.*
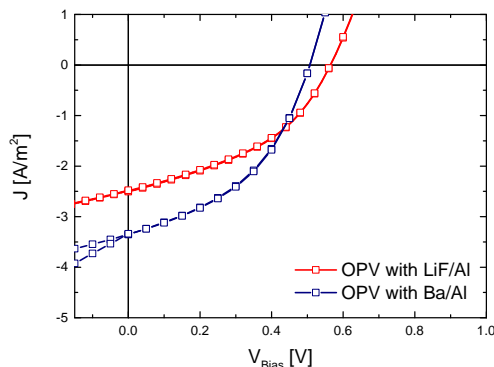
Figure 3.16: *Room-temperature J-V characteristics of solar cells with a P3HT:PDI-1 (1:3 wt/wt) system and with LiF/Al (red) and Ba/Al (blue) as cathode.*

Table 3.8: *Comparison of the figures of merit of the non-annealed P3HT:PDI-1 (1:3 wt/wt) solar cells with a LiF/Al and Ba/Al cathode.*

Device cathode	Thickness [nm]	V_{OC} [V]	J_{SC} [A/m²]	FF [%]	PCE [%]
Ba/Al	105	0.49 ±0.05	2.47 ±0.88	40.38 ±3.08	0.055 ±0.028
LiF/Al	190	0.56 ±0.01	2.12 ±0.37	41.35 ±1.80	0.055 ±0.011

Figure 3.16 and table 3.8 shows the comparison between the non-annealed devices of P3HT:PDI-1 (1:3 wt/wt) with Ba/Al and LiF/Al as a cathode. The devices with a Ba/Al cathode shows a higher J_{SC} maximum value which yielded a PCE of 0.083 %, compared to the maximum PCE of 0.066 % of the devices with the LiF/Al cathode. However the latter had a much more working areas and better reproducibility of these (see figures A10a and A10b). Overall the devices with a LiF/Al cathode have higher V_{OC} while devices with a Ba/Al cathode show a higher J_{SC}. Coincidentally, this results in the Ba/Al and LiF/Al devices having the same average power conversion efficiency.

3.3 PDI derivatives

As mentioned previously, traditional PDI derivatives show over-strong aggregation which severely limits the conversion efficiency of solar cells. PDI derivatives were synthesized and provided by the group of Prof. Müllen from MPIP, with the aim of reducing planarity and therefore over-aggregation. Due to confidentiality reasons, the exact structure of these PDI derivatives cannot be disclosed. However it can be said that they are simple PDI derivatives with small changes/additions in the aforementioned possible tailoring positions (figure 1.7, chapter 1).

PDI-2

Electron-only devices were fabricated with a P3HT:PDI-2 (1:1 wt/wt) blend in chloroform (6.67 mgml⁻¹) as active layer. The active blend was spin coated at 1200 rpm for a layer thickness of around 75 nm. One batch of devices was pre annealed and the other post annealed at 120°C for 10 minutes, and both were topped off with a Ba/Al cathode.
In figure 3.17a, the comparison of the *J-V* characteristics of non-annealed, pre annealed and post-annealed EO devices is presented. Non-annealed and pre annealed devices show significant asymmetries in their electron current profiles, resulting from poor electron injection from the

(Al$_2$O$_3$) and Ba/Al side, respectively. This is not true in post annealed devices where a much more balanced electron current is visible across the layer, indicating that thermal annealing after cathode evaporation is optimizing the interfaces between the contact and the active layer and, therefore, optimizing electron injection. This is further evidenced by the more quadratic dependence on voltage at forward bias of the post annealed EO device, which can again be seen more clearly in figure 3.17b. As depicted, the electron current for the post annealed device can be satisfactorily described by the SCLC model (eq.1.1), while for the pre annealed devices, and even more so for the non-annealed EO devices, the current current starts to deviate from the quadratic voltage dependence due to the already mentioned influence of carrier injection from the contact. To better verify for bulk limited currents and retrieve correct mobility values, thickness dependent measurements of the *J-V* characteristics and their fitting are required.

Figure 3.18 shows the temperature dependent *J-V* characteristics of the EO devices. The fits are obtained through Pasveer's model using the set of parameters presented in table 3.11. For both pre and post annealed EO devices, the temperature dependent electron current could be well described with a single set of parameters, which did not happen for the non-annealed device due to the much more limited injection current behaviour. The mobility retrieved from the unified description of Pasveer, was 1.18 x 10^{-15} m^2/Vs, 2.83 x 10^{-16} m^2/Vs and 1.96 x 10^{-13} m^2/Vs. This preliminary results, with the fairly good agreement of the current-voltage characteristics through eq.1.1 and the accurate description of the data with the drift-diffusion model, are indications that the electron transport in PDI-2 is trap free. However, electron currents in PDI-2 are far below (about one order of magnitude) the currents obtained in PDI-1 based EO devices.

(a)   (b)
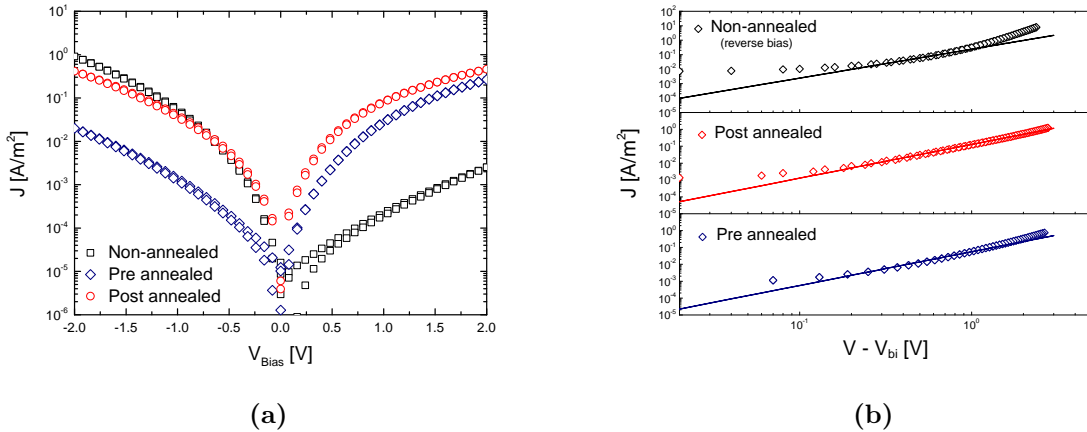
Figure 3.17: *(a) Experimental J-V characteristics of non-annealed (red), pre annealed (green) and post annealed (blue) EO devices with a P3HT:PDI-2 (1:1 wt/wt) active layer, with thickness of ∼75 nm. (b) Fitting (solid lines) of the electron currents (symbols) with eq.1.1 for SCLC.*

(a)

(b)

(c)
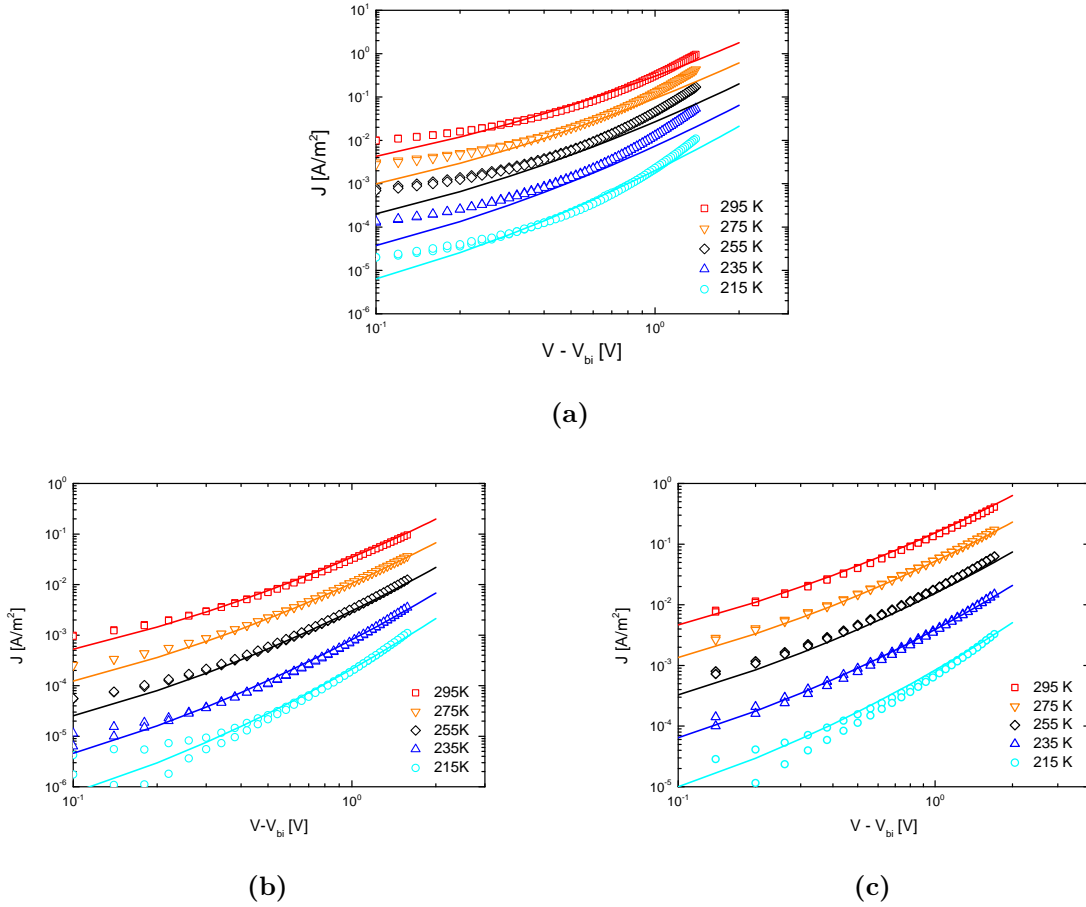
Figure 3.18: *Temperature dependent experimental J-V characteristics (symbols) of P3HT:PDI-2 (1:1 wt/wt) (a) non-annealed, (b) pre annealed and (c) post annealed EO devices, with a layer thickness of ∼75 nm. The solid lines are fits to the experimental data, obtained with Pasveer's model.*

Table 3.9: *Fit parameters used for modelling the temperature-dependent J-V characteristics of a non-annealed and annealed P3HT:PDI-2 (1:1 wt/wt) EO device with a layer thickness of ∼75 nm.*

Device	μ_0 (295 K)	Mobility pre-factor	Width of Gaussian, σ	Site spacing, a	Φ left/right	V_{bi}
Non-annealed	1.18×10^{-15} m²/Vs	3000	0.185 eV	1.2 nm	0/3 eV	0.6 V
Pre annealed	2.83×10^{-16} m²/Vs	220	0.18 eV	1.2 nm	0/3 eV	0.4 V
Post annealed	1.96×10^{-13} m²/Vs	9	0.132 eV	1.6 nm	0/3 eV	0.3 V

PDI-3

Electron-only devices were fabricated with a P3HT:PDI-3 system with two different PDI ratios: 1:1 (wt/wt) and 1:1.5 (wt/wt) P3HT:PDI-3, in chloroform. The active blends were spin coated for layer thicknesses of ∼110 nm and ∼130 nm, respectively. The (1:1 wt/wt) electron-only devices were pre annealed (5 min at 120°C) and the (1:1.5 wt/wt) electron-only devices were post annealed (30 min at 100°C). Their *J-V* characteristics are shown in figure 3.19 (P3HT:PDI-3 (1:1 wt/wt) EO devices) and figure 3.20 (P3HT:PDI-3 (1:1.5 wt/wt) EO devices). The slight change of PDI ratio, as well as the different annealing process, results in overall electron currents of the same order, albeit with a reversed current profile. On the other hand, thermal treatment of the cathode resulted in a significant drop of the current from the Ba/Al side, now clearly injection limited. This contrasts with the previous experiments where the post annealing has

the opposite effect and improves injection from the top contact, and may be justified by the significantly higher annealing time of 30 min that seems to be "damaging" the interface between cathode and active layer. As a result, a deeply unbalanced electron transport across the layer is observed. The electron currents of both ((1:1 wt/wt) and (1:1.5 wt/wt)) P3HT:PDI-3 EO devices, exhibit a quadratic dependence on voltage in the range of applied bias used and can therefore be well described by eq.1.1. Unfortunately, temperature scan was only performed for the non-annealed devices with a P3HT:PDI-1 (1:1) ratio. These temperature dependent *J-V* characteristics are presented in figure 3.21. As can be observed, the temperature dependent electron current could be well described through the drift-diffusion model from Pasveer, with a single set of parameters, which can be found in table 3.10. The extracted electron mobility was $\sim 2.53 \times 10^{-14}$ m^2/Vs. The good agreement of the current-voltage characteristics with eq.1.1 and the accurate description of the data with the numerical simulations are indications that the electron transport in PDI-3 is essentially trap free. The electron current observed for PDI-3 are at the same level of the one obtained with PDI-1, but still relatively low. Hole-only devices should be characterized to verify the behaviour of hole transport in PDI-3 as well as a P3HT:PDI-3 (1:3 wt/wt) ratio should be tried for further comparison with the fabricated PDI-1 devices.
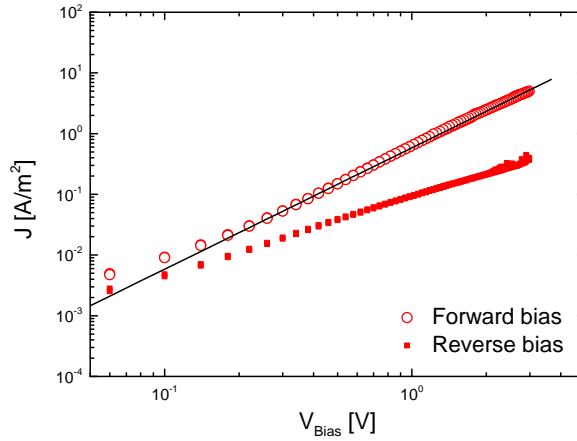
Figure 3.19: *Experimental J-V characteristics (symbols) of a pre annealed P3HT:PDI-3 (1:1 wt/wt) electron-only device, with an active layer thickness of ∼110 nm. The solid lines are fits to the experimental data, calculated with eq.1.1 for SCLC.*

(a)

(b)
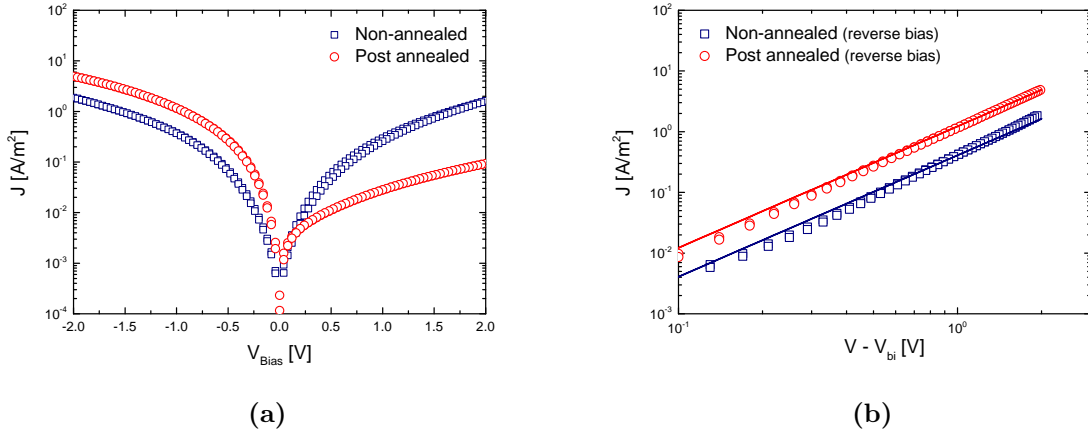
Figure 3.20: *Experimental J-V characteristics (symbols) of a P3HT:PDI-3 (1:1.5 wt/wt) non-annealed (bue) and post annealed (red) EO device, with an active layer thickness of ∼130 nm. The solid lines are fits to the experimental data, calculated with eq.1.1 for SCLC. A V_{bi} of 0.05 V was used for the non-annealed device.*
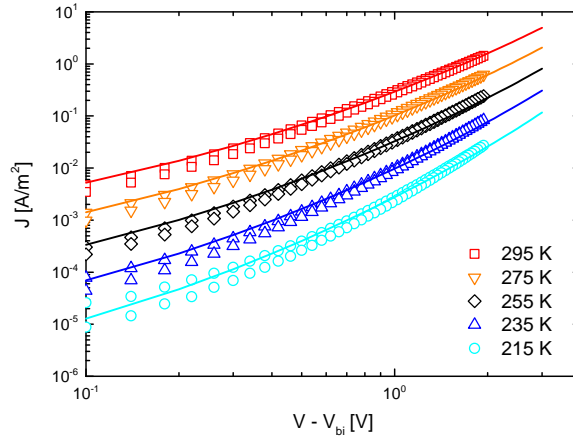
Figure 3.21: *Temperature dependent J-V characteristics (symbols) of a non-annealed P3HT:PDI-3 (1:1.5 wt/wt) EO device, with an active layer thickness of ∼130 nm. The solid lines are the fits to the experimental data, calculated with Pasveer's model (eq.1.3).*

Table 3.10: *Fit parameters used for modelling the temperature-dependent J-V characteristics of a non-annealed P3HT:PDI-3 (1:1.5 wt/wt) EO device with a layer thickness of ∼130 nm.*

Device	μ_0 (295 K)	Mobility pre-factor	Width of Gaussian, σ	Site spacing, a	Φ left/right	V_{bi}
Non-annealed	2.53 x 10^{-14} m²/Vs	360	0.16 eV	1.8 nm	0/3 eV	0.06 V

PDI-4

Another PDI derivative was also tested. Electron-only devices were fabricated using PDI derivative number 4 in a P3HT:PDI-4 (1:1 wt/wt) blend in chloroform, with both a Ba/Al cathode and a LiF/Al one. Devices were post annealed at 120°C for 10 minutes.

In figures 3.22b and 3.23b, are presented the *J-V* characteristics of the EO devices with a Ba/Al and LiF/Al cathode, respectively. Electron currents from the devices with a LiF/Al cathode

27

are about 2 orders of magnitude higher, showing the improved injection from this material. The *J-V* characteristics of the non-annealed devices of either batch, for the applied bias range, look to be limited by carrier injection from the contacts. Post annealing of the devices with Ba/Al, caused a symmetric current drop across the layer whilst for the devices with LiF, it seems that the current becomes more balanced across the layer and that the injection limited behaviour reduces to a slightly more quadratic dependence on voltage. Therefore, the electron current of the post annealed device can still be satisfactorily described with eq.1.1 (figure 3.23b). Non-annealed EO devices however, have a more pronounced injection behaviour and deviation from quadratic dependence on voltage at higher applied voltages, and therefore its experimental *J-V* characteristics could not be accurately described by eq.1.1. This was also the case in the modelling of the temperature scans made, as depicted in figure 3.24, where a good fit that describes the temperature dependent *J-V* characteristics of the non-annealed EO device was not possible. The temperature dependent electron current of the post annealed EO device, on the other hand, could be well described with a single set of parameters, through the drift-diffusion model, shown in table 3.11. The extracted electron mobilities were 8.65 x 10^{-16} m^2/Vs and 1.96 x 10^{-13} m^2/Vs. Once again, this observations point to electron trap-free transport in P3HT:PDI-4 blend films.

(a)   **(b)**
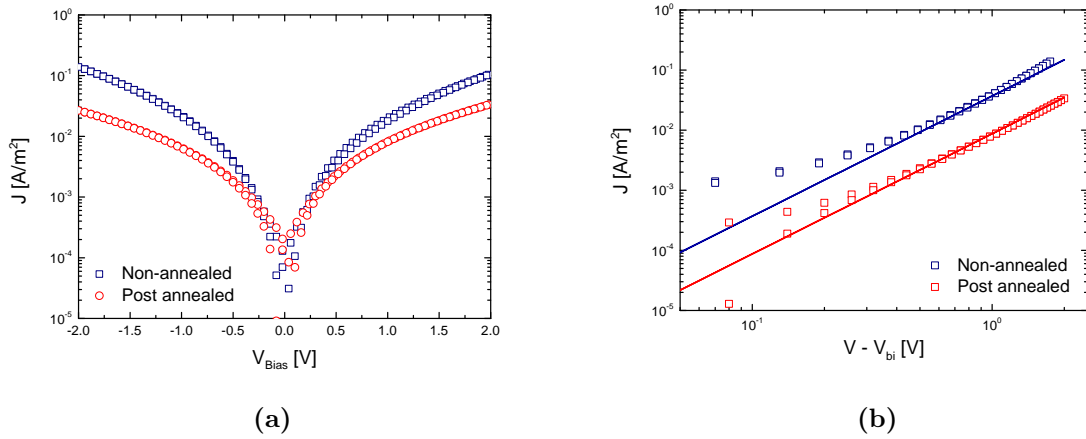
Figure 3.22: *Experimental J-V characteristics (symbols) of a P3HT:PDI-4 (1:1 wt/wt) EO device, non-annealed (bue) and post annealed (red), with a Ba/Al cathode with and an active layer thickness of ~190 nm. The solid lines are fits to the experimental data, calculated with eq.1.1 for SCL currents, while the dashed lines are linear fits with slope 1 that delimit the ohmic region of the current. For the non-annealed device, a V_{bi} of 0.2 V was used.*

(a)

(b)
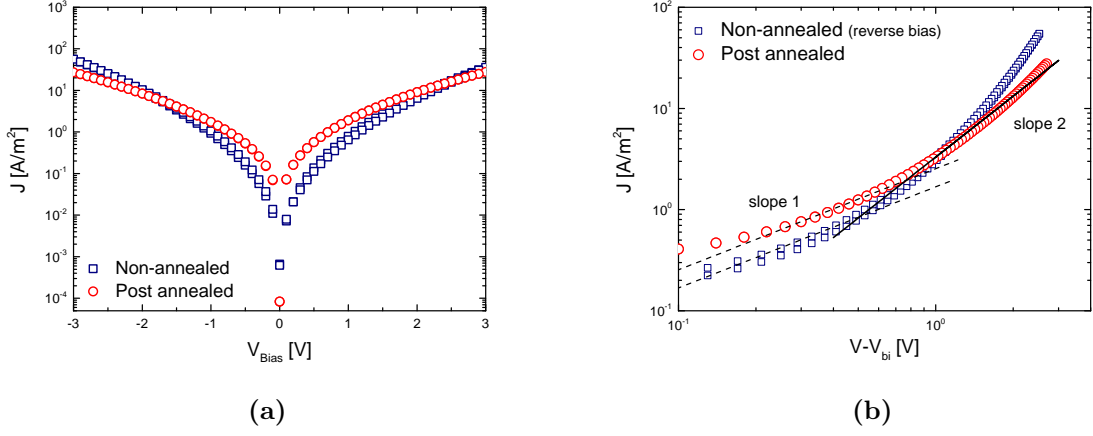
Figure 3.23: *Experimental J-V characteristics (symbols) of a P3HT:PDI-4 (1:1 wt/wt) EO device, non-annealed (bue) and post annealed (red), with a LiF/Al cathode with and an active layer thickness of ∼95 nm. The solid lines are fits to the experimental data, calculated with eq.1.1 for SCL currents, while the dashed lines are linear fits with slope 1 that delimit the ohmic region of the current. A V_{bi} of 0.3 V was used.*

(a)

(b)
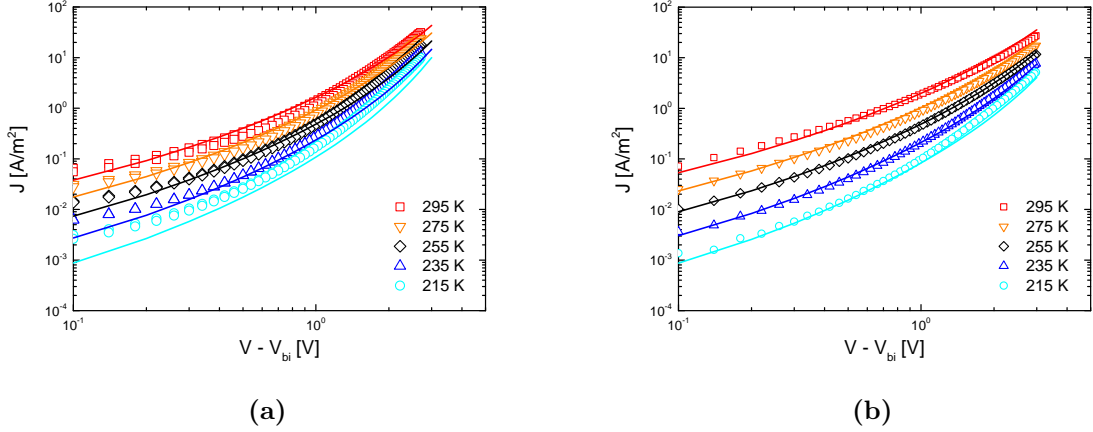
Figure 3.24: *Temperature dependent J-V characteristics (symbols) of P3HT:PDI-4 (1:1 wt/wt) (a) non-annealed and (b) post annealed EO devices. The solid lines are fits to the experimental data, obtained with Pasveer's model.*

Table 3.11: *Fit parameters used for modelling the temperature-dependent J-V characteristics of the non- pre- and post annealed P3HT:PDI-4 (1:1 wt/wt) EO devices, with a LiF/Al cathode and an active layer thickness of ∼95 nm.*

Device	μ_0 (295 K)	Mobility pre-factor	Width of Gaussian, σ	Site spacing, a	Φ left/right	V_{bi}
Non-annealed	8.65 x 10^{-16} m²/Vs	2800	0.186 eV	1.05 nm	0/3 eV	0.45 V
Post annealed	1.96 x 10^{-13} m²/Vs	9	0.132 eV	1.6 nm	0/3 eV	0.3 V

Conclusions and future perspectives

P3HT:PCBM (1:1 wt/wt) solar cells have been fabricated. These OPVs , in terms of power conversion efficiency, fell short when compared to identical devices based on the same system, without any additive or additional material layers. New attempts should be made in order to serve as a proper reference cell in our working conditions. Also as previously mentioned, the ideality factor from light output needs to be retrieved in order to get a more reliable value and conclusions about the recombination process.

Regarding the PDI based devices, a first observation is that all the electron currents, J_{SC} values and PCEs of the fabricated devices with PDI-1 are n general really low compared to the expected. A fellow research group within the MPIP, had previously fabricated (commercial) PDI-1 based solar cells with a P3HT:PDI-1 (1:1 wt/wt) ratio where a J_{SC} of 14.9 m²/Vs and a PCE of 0.25 % were obtained [45]. Following the same processing steps we achieved a PCE of only 0.024 %. We believe that such discrepancy may well be attributed to us being using an older batch lot of material (specifically PDI-1), to variations of material batches themselves and to the area power density of the solar simulator used. However, high power conversion efficiencies was never the main objective of this work, but rather getting a more comprehensive understanding of the material electronic properties and charge transport characteristics of these materials, as well as to observe the effect of different processing conditions and thermal annealing on the devices.

The absolute first order of work would have to be making a series of measurements of the J-V characteristics for a range of different thicknesses, for all the EO device systems presented here with the different PDIs (commercial PDI-1 and the PDI derivatives). Preliminary results from different blend ratios of P3HT:PDI-1 (1:1) and (1:3) indicate the presence of an electron trap free transport and show an increase in the device performance with increasing PDI-1 ratio . Electron current from single carrier devices increases an order of magnitude and in the non-annealed solar cells with a LiF/Al cathode (with a P3HT:PDI ration of 1:1 and 1:3), and we observe that same increase difference in the current density and power conversion efficiency. The J-V characteristics of (post) annealed P3HT:PDI-1 (1:3 wt/wt) solar cells, with LiF/Al cathode, must still be measured, however, as the non-annealed devices yielded the highest current density and PCE values.

With exception of the MEH-PPV:PDI-1 devices, thermal annealing resulted in a strong effect in normal structure solar cells that decreased V_{OC}, but increased J_{SC} and overall device performance. This is generally because annealing promotes a certain amount od PDI crystallization that improves long range order, lateral phase separation and increase interfacial area that facilitates charge separation and provides slightly better percolation pathways. This helps balancing charge transport and currents across the device layer and therefore improve J_{SC}. Post annealing also helps removing any interfacial states between the active layer and the metal contacts improving charge collection and reducing recombination. From J-V characteristics of the P3HT:PDI-1 (1:1 wt/wt) solar cells with a Ba/Al cathode top contact experiment, where both post annealing and pre annealing were done, we conclude that post annealing results in a higher increase in J_{SC} and that the thermal treatment of the top contact is not responsible for the V_{OC} loss. Post annealing also helps removing any interfacial states between the active layer and the top metal contact improving charge collection and reducing recombination. P3HT:PDI-1 (1:1 wt/wt) solar cells with LiF/Al as cathode present higher J_{SC} values, compared with when a Ba/Al is used, which is associated with the thinner LiF layer and the better interfacial structural arrangement between the contact and the active layer.

Morphological studies show that over-aggregation in PDI blends is still a big problem, which

hinders charge carrier transport and performance in solar cells. Further studies will hopefully help to better correlate blend film structure and phase separation, with their charge transport properties.

Initial tests on these three PDI derivatives also indicate electron trap free transport, albeit with much lower current values. Due to the limited amount of material available of PDI derivatives and time, so was the number of experiments that were done, which did not allow for the repetition of experiments. Therefore it is not possible to infer about reproducibility of the results and retrieve further conclusions from the approximated values of the site spacing and energetic disorder of the active blend obtained from the modelling of the temperature-dependent *J-V* characteristics.

Bibliography

[1] G. Yu, J. Gao, J. C. Hummelen, F. Wudl, and A. J. Heeger. Polymer photovoltaic cells: Enhanced efficiencies via a network of internal donor-acceptor heterojunctions. *Science*, 270(5243):1789–1791, 1995.

[2] Gang Li, Vishal Shrotriya, Jinsong Huang, Yan Yao, Tom Moriarty, Keith Emery, and Yang Yang. High-efficiency solution processable polymer photovoltaic cells by self-organization of polymer blends. *Nature materials*, 4(11):864–868, 2005.

[3] Gang Li, Rui Zhu, and Yang Yang. Polymer solar cells. *Nature Photonics*, 6(3):153–161, 2012.

[4] Jae Kwan Lee, Wan Li Ma, Christoph J Brabec, Jonathan Yuen, Ji Sun Moon, Jin Young Kim, Kwanghee Lee, Guillermo C Bazan, and Alan J Heeger. Processing additives for improved efficiency from bulk heterojunction solar cells. *Journal of the American Chemical Society*, 130(11):3619–3623, 2008.

[5] Jingbi You, Letian Dou, Ken Yoshimura, Takehito Kato, Kenichiro Ohya, Tom Moriarty, Keith Emery, Chun-Chao Chen, Jing Gao, Gang Li, et al. A polymer tandem solar cell with 10.6% power conversion efficiency. *Nature communications*, 4:1446, 2013.

[6] Zhicai He, Chengmei Zhong, Shijian Su, Miao Xu, Hongbin Wu, and Yong Cao. Enhanced power-conversion efficiency in polymer solar cells using an inverted device structure. *Nature Photonics*, 6(9):591–595, 2012.

[7] Martijn Kuik, Gert-Jan AH Wetzelaer, Herman T Nicolai, N Irina Craciun, Dago M De Leeuw, and Paul WM Blom. 25th anniversary article: Charge transport and recombination in polymer light-emitting diodes. *Advanced Materials*, 26(4):512–531, 2014.

[8] Allen Miller and Elihu Abrahams. Impurity conduction at low concentrations. *Physical Review*, 120(3):745, 1960.

[9] H Bässler. Charge transport in disordered organic photoconductors. *phys. status solidi b*, 175(1):15–56, 1993.

[10] Cristina Tanase. *Unified charge transport in disordered organic field-effect transistors and light-emitting diodes*. [University Library Groningen][Host], 2005.

[11] Gert-Jan Wetzelaer. *Charge Transport and Recombination in Organic-Semiconductor Diodes*. PhD thesis, University of Groningen, 2014.

[12] Murray A Lampert and Peter Mark. *Current injection in solids*. Academic Press, 1970.

[13] Nevill Francis Mott and Ronald Wilfrid Gurney. *Electronic processes in ionic crystals*. Clarendon Press, 1948.

[14] J.J. Brondijk. *Thickness dependent mobility of MEH-PPV and towards multi-layer PLEDs*. [University Library Groningen][Host], 2006.

[15] WF Pasveer, Jeroen Cottaar, C Tanase, Reinder Coehoorn, PA Bobbert, PWM Blom, DM De Leeuw, and MAJ Michels. Unified description of charge-carrier mobilities in disordered semiconducting polymers. *Physical review letters*, 94(20):206601, 2005.

[16] Roland Schmechel and Heinz Von Seggern. Electronic traps in organic transport layers. *Physica status solidi (a)*, 201(6):1215–1235, 2004.

[17] HT Nicolai, M Kuik, GAH Wetzelaer, B De Boer, C Campbell, C Risko, JL Brédas, and PWM Blom. Unification of trap-limited electron transport in semiconducting polymers. *Nature materials*, 11(10):882–887, 2012.

[18] M Kuik, LJA Koster, GAH Wetzelaer, and PWM Blom. Trap-assisted recombination in disordered organic semiconductors. *Physical review letters*, 107(25):256805, 2011.

[19] P Langevin. Recombinaison et mobilites des ions dans les gaz. *Ann. Chim. Phys*, 28(433):122, 1903.

[20] Martin Pope and Charles E Swenberg. *Electronic processes in organic crystals and polymers*. Oxford University Press on Demand, 1999.

[21] Xiaowei Zhan, Antonio Facchetti, Stephen Barlow, Tobin J Marks, Mark A Ratner, Michael R Wasielewski, and Seth R Marder. Rylene and related diimides for organic electronics. *Advanced Materials*, 23(2):268–284, 2011.

[22] Chun Huang, Stephen Barlow, and Seth R Marder. Perylene-3, 4, 9, 10-tetracarboxylic acid diimides: Synthesis, physical properties, and use in organic electronics. *The Journal of organic chemistry*, 76(8):2386–2407, 2011.

[23] Lukas Schmidt-Mende, Andreas Fechtenkötter, Klaus Müllen, Ellen Moons, Richard H Friend, and JD MacKenzie. Self-organized discotic liquid crystals for high-efficiency organic photovoltaics. *Science*, 293(5532):1119–1122, 2001.

[24] Chen Li and Henrike Wonneberger. Perylene imides for organic photovoltaics: yesterday, today, and tomorrow. *Advanced Materials*, 24(5):613–636, 2012.

[25] Ian A Howard, Frederic Laquai, Panagiotis E Keivanidis, Richard H Friend, and Neil C Greenham. Perylene tetracarboxydiimide as an electron acceptor in organic solar cells: a study of charge generation and recombination. *The Journal of Physical Chemistry C*, 113(50):21225–21232, 2009.

[26] Xin Zhang, Zhenhuan Lu, Long Ye, Chuanlang Zhan, Jianhui Hou, Shaoqing Zhang, Bo Jiang, Yan Zhao, Jianhua Huang, Shanlin Zhang, et al. A potential perylene diimide dimer-based acceptor material for highly efficient solution-processed non-fullerene organic solar cells with 4.03% efficiency. *Advanced Materials*, 25(40):5791–5797, 2013.

[27] Yuze Lin, Yifan Wang, Jiayu Wang, Jianhui Hou, Yongfang Li, Daoben Zhu, and Xiaowei Zhan. A star-shaped perylene diimide electron acceptor for high-performance organic solar cells. *Advanced Materials*, 26(30):5137–5142, 2014.

[28] Dian Chen, Atsuhiro Nakahara, Dongguang Wei, Dennis Nordlund, and Thomas P Russell. P3ht/pcbm bulk heterojunction organic photovoltaics: correlating efficiency and morphology. *Nano letters*, 11(2):561–567, 2010.

[29] Gilles Dennler, Markus C Scharber, Christoph J Brabec, et al. Polymer-fullerene bulk-heterojunction solar cells. *Adv. Mater*, 21(13):1323–1338, 2009.

[30] Girish Lakhwani, Akshay Rao, and Richard H Friend. Bimolecular recombination in organic photovoltaics. *Annual review of physical chemistry*, 65:557–581, 2014.

[31] Sarah R Cowan, Anshuman Roy, and Alan J Heeger. Recombination in polymer-fullerene bulk heterojunction solar cells. *Physical Review B*, 82(24):245207, 2010.

[32] Gert-Jan AH Wetzelaer and Paul WM Blom. Diffusion-driven currents in organic-semiconductor diodes. *NPG Asia Materials*, 6(7):e110, 2014.

[33] Thomas Kirchartz, Florent Deledalle, Pabitra Shakya Tuladhar, James R Durrant, and Jenny Nelson. On the differences between dark and light ideality factor in polymer: fullerene solar cells. *The Journal of Physical Chemistry Letters*, 4(14):2371–2376, 2013.

[34] Ravichandran Shivanna, Safa Shoaee, Stoichko Dimitrov, Sunil Kumar Kandappa, Sridhar Rajaram, James R Durrant, and KS Narayan. Charge generation and transport in efficient organic bulk heterojunction solar cells with a perylene acceptor. *Energy & Environmental Science*, 7(1):435–441, 2014.

[35] Jonathan Rivnay, Leslie H Jimison, John E Northrup, Michael F Toney, Rodrigo Noriega, Shaofeng Lu, Tobin J Marks, Antonio Facchetti, and Alberto Salleo. Large modulation of carrier transport by grain-boundary molecular packing and microstructure in organic thin films. *Nature materials*, 8(12):952–958, 2009.

[36] Jeroen KJ van Duren, Xiaoniu Yang, Joachim Loos, Corrie WT Bulle-Lieuwma, Alexander B Sieval, Jan C Hummelen, and René AJ Janssen. Relating the morphology of poly (p-phenylene vinylene)/methanofullerene blends to solar-cell performance. *Advanced Functional Materials*, 14(5):425–434, 2004.

[37] Sean E Shaheen, Christoph J Brabec, N Serdar Sariciftci, Franz Padinger, Thomas Fromherz, and Jan C Hummelen. 2.5% efficient organic plastic solar cells. *Applied Physics Letters*, 78(6):841–843, 2001.

[38] NI Craciun, JJ Brondijk, and PWM Blom. Diffusion-enhanced hole transport in thin polymer light-emitting diodes. *Physical Review B*, 77(3):035206, 2008.

[39] AA Grinberg and Serge Luryi. Space-charge-limited current and capacitance in double-junction diodes. *Journal of applied physics*, 61(3):1181–1189, 1987.

[40] A Wagenpfahl, D Rauh, M Binder, C Deibel, and V Dyakonov. S-shaped current-voltage characteristics of organic solar devices. *Physical Review B*, 82(11):115306, 2010.

[41] Thomas Kirchartz, Tiziano Agostinelli, Mariano Campoy-Quiles, Wei Gong, and Jenny Nelson. Understanding the thickness-dependent performance of organic bulk heterojunction solar cells: the influence of mobility, lifetime, and space charge. *The Journal of Physical Chemistry Letters*, 3(23):3470–3475, 2012.

[42] VD Mihailetchi, J Wildeman, and PWM Blom. Space-charge limited photocurrent. *Physical review letters*, 94(12):126602, 2005.

[43] Mingguang Li, Lei Wang, Jiangang Liu, Ke Zhou, Xinhong Yu, Rubo Xing, Yanhou Geng, and Yanchun Han. Cooperative effects of solvent and polymer acceptor co-additives in p3ht: Pdi solar cells: simultaneous optimization in lateral and vertical phase separation. *Physical Chemistry Chemical Physics*, 16(10):4528–4537, 2014.

[44] Craig H Peters, IT Sachs-Quintana, William R Mateker, Thomas Heumueller, Jonathan Rivnay, Rodrigo Noriega, Zach M Beiley, Eric T Hoke, Alberto Salleo, and Michael D McGehee. The mechanism of burn-in loss in a high efficiency polymer solar cell. *Advanced Materials*, 24(5):663–668, 2012.

[45] Valentin Kamm, Glauco Battagliarin, Ian A Howard, Wojciech Pisula, Alexey Mavrinskiy, Chen Li, Klaus Müllen, and Frédéric Laquai. Polythiophene: Perylene diimide solar cells–the impact of alkyl-substitution on the photovoltaic performance. *Advanced Energy Materials*, 1(2):297–302, 2011.
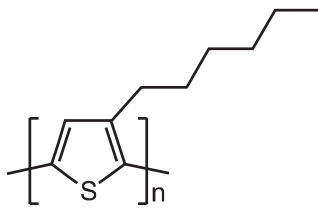
Auxiliary Figures

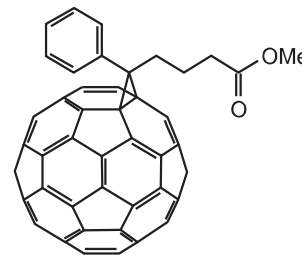**Materials and methods**
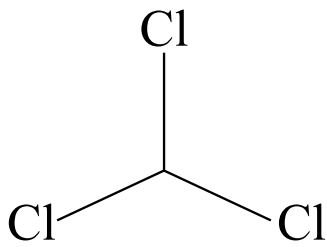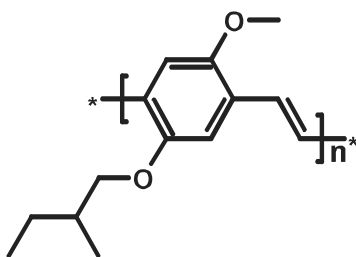

(a) *Trichloromethane (Chloroform)*
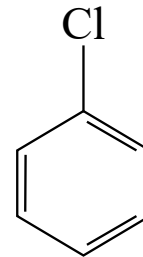
(b) *Chlorobenzene*

Figure A1: *Illustration of the chemical structure of the solution solvents Chloroform and Chlorobenzene.*
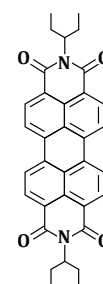

(a) *P3HT*
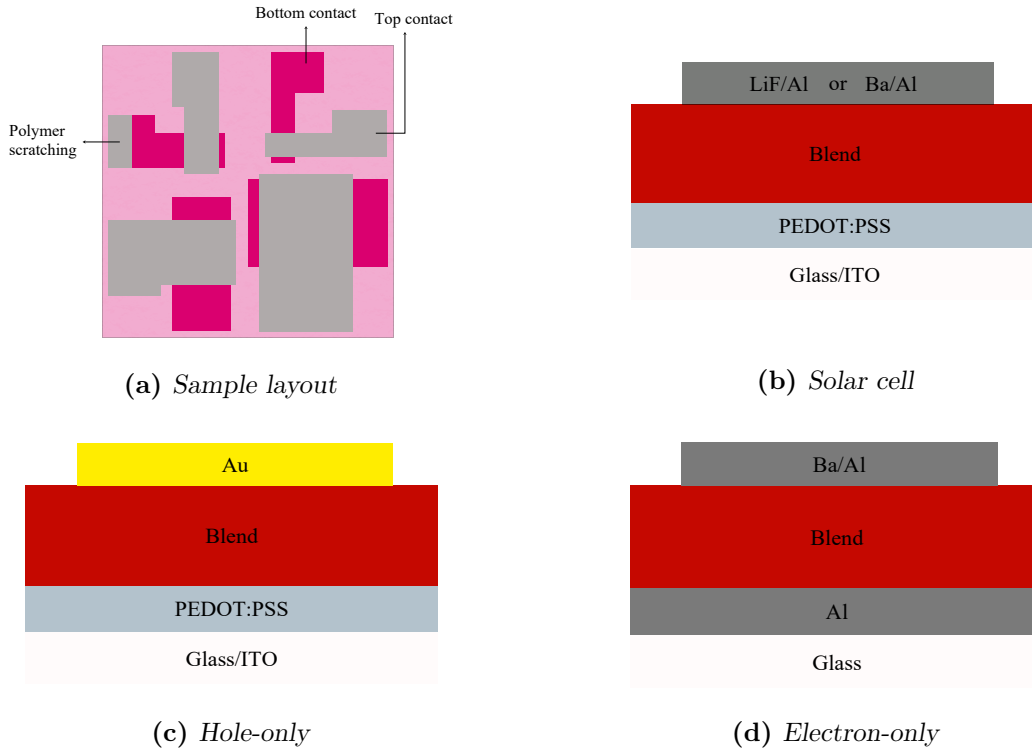

**(b)** *PCBM*

(c) *MEH-PPV*

(d) *Commercial PDI-1*

Figure A2: *Illustration of the chemical structure of the donor materials P3HT and MEH-PPV and the acceptor materials Commercial PDI-1 and PCBM.*

(a) *Sample layout*

(b) *Solar cell*

(c) *Hole-only*

(d) *Electron-only*

Figure A3: *(a) Schematic representation of a device sample, top view. Illustration of the solar cell, electron-only and hole-only device structures used for this work.*


Figure A4: *Picture of a Vactec thermal evaporation system. This system allows for the evaporation of a number of different metals, under a typical pressure of around 5 x 10^{-7} mbar, supporting up to 9 samples at a time.*
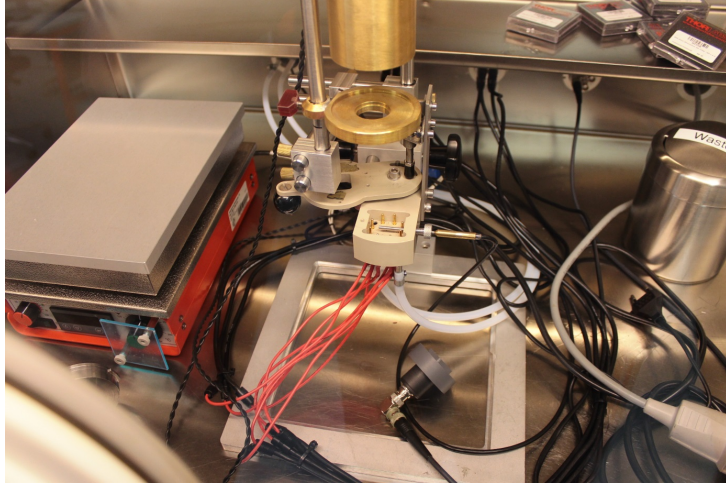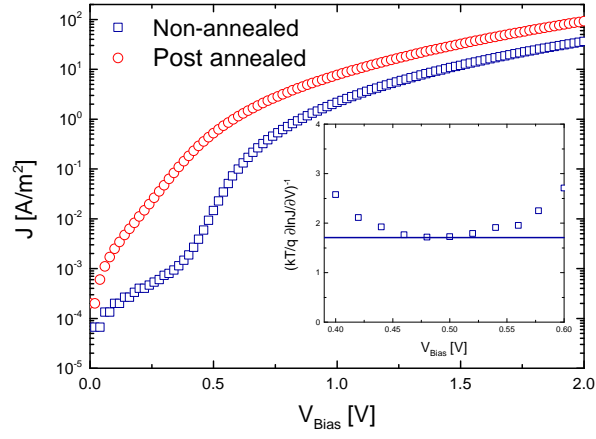
Figure A5: *Picture of the I-V setup, put together at MPIP. The system allows for the control of the device temperature via liquid nitrogen.*
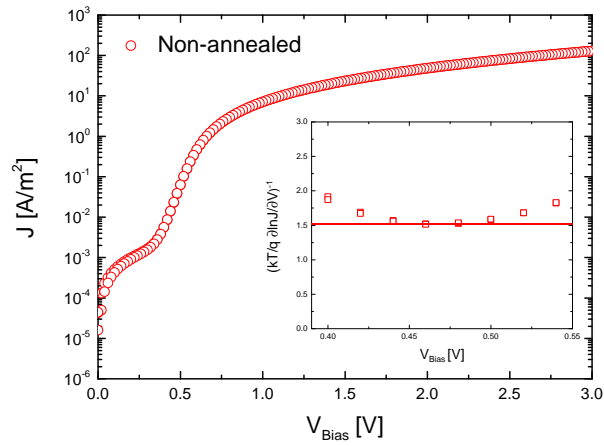
Results and Discussion
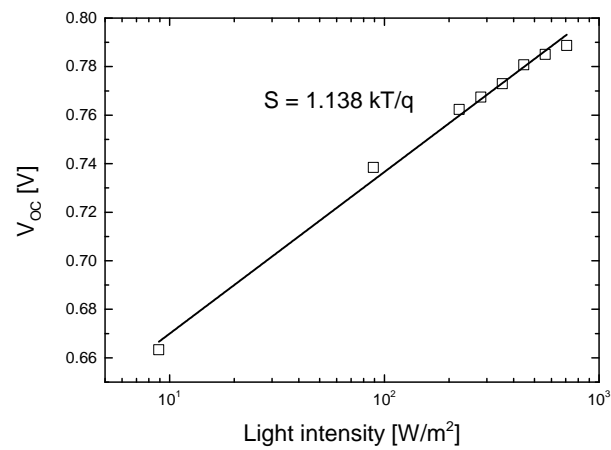
Figure A6: *Light intensity dependence of V_{OC} of a non-annealed MEH-PPV:PDI-1 (1:4 wt/wt) solar cell.*

Figure A7: *Dark current characteristics at forward bias of a non-annealed (blue) and post annealed (red) P3HT:PDI-1 (1:1 wt/wt) solar cell . The inset shows the differential plot of the data according to equation 3.1.*

Figure A8: *Dark current characteristics at forward bias of a non-annealed P3HT:PDI-1 (1:3 wt/wt) solar cell. The inset shows the differential plot of the data according to equation 3.1.*
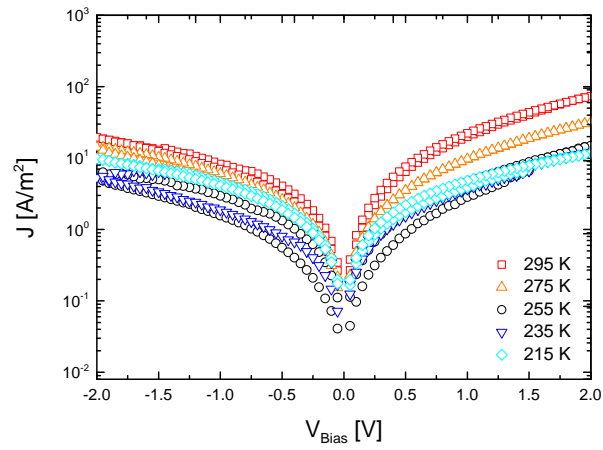
Figure A9: *Temperature dependent experimental J-V characteristics (symbols) of a P3HT:PDI-1 (1:3 wt/wt) EO device.*

(a)

(b)
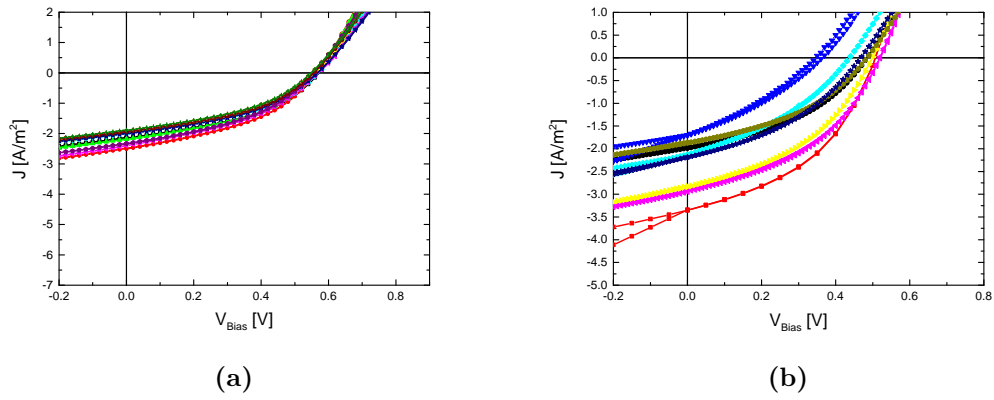
Figure A10: *Experimental J-V characteristics of all working areas of P3HT:PDI-1 (1:3 wt/wt) solar cells with a cathode of (a) LiF/Al and (b) Ba/Al.*